Monthly Notices
of the
ROYAL ASTRONOMICAL SOCIETY

MNRAS **467,** 2019–2038 (2017) doi:10.1093/mnras/stx147
Advance Access publication 2017 January 25

# The stellar mass–halo mass relation of isolated field dwarfs: a critical test of ΛCDM at the edge of galaxy formation

J. I. Read,[1⋆] G. Iorio,[2,3] O. Agertz[1] and F. Fraternali[2,4]

[1] *Department of Physics, University of Surrey, Guildford, Surrey GU2 7XH, UK*
[2] *Dipartimento di Fisica e Astronomia, Università di Bologna, Viale Berti Pichat 6/2, I-40127, Bologna, Italy*
[3] *INAF – Osservatorio Astronomico di Bologna, via Ranzani 1, I-40127, Bologna, Italy*
[4] *Kapteyn Astronomical Institute, University of Groningen, Landleven 12, NL-9747 AD Groningen, the Netherlands*

Accepted 2017 January 17. Received 2016 December 6; in original form 2016 July 11

## ABSTRACT

We fit the rotation curves of isolated dwarf galaxies to directly measure the stellar mass–halo mass relation ($M_\star$–$M_{200}$) over the mass range $5 \times 10^5 \lesssim M_\star/\mathrm{M}_\odot \lesssim 10^8$. By accounting for cusp-core transformations due to stellar feedback, we find a monotonic relation with little scatter. Such monotonicity implies that abundance matching should yield a similar $M_\star$–$M_{200}$ if the cosmological model is correct. Using the 'field galaxy' stellar mass function from the Sloan Digital Sky Survey (SDSS) and the halo mass function from the Λ cold dark matter Bolshoi simulation, we find remarkable agreement between the two. This holds down to $M_{200} \sim 5 \times 10^9$ $\mathrm{M}_\odot$, and to $M_{200} \sim 5 \times 10^8$ $\mathrm{M}_\odot$ if we assume a power-law extrapolation of the SDSS stellar mass function below $M_\star \sim 10^7$ $\mathrm{M}_\odot$. However, if instead of SDSS we use the stellar mass function of nearby galaxy groups, then the agreement is poor. This occurs because the group stellar mass function is shallower than that of the field below $M_\star \sim 10^9$ $\mathrm{M}_\odot$, recovering the familiar 'missing satellites' and 'too big to fail' problems. Our result demonstrates that both problems are confined to group environments and must, therefore, owe to 'galaxy formation physics' rather than exotic cosmology. Finally, we repeat our analysis for a Λ Warm Dark Matter cosmology, finding that it fails at 68 per cent confidence for a thermal relic mass of $m_{\mathrm{WDM}} < 1.25$ keV, and $m_{\mathrm{WDM}} < 2$ keV if we use the power-law extrapolation of SDSS. We conclude by making a number of predictions for future surveys based on these results.

**Key words:** galaxies: dwarf – galaxies: irregular – galaxies: kinematics and dynamics – Local Group – cosmological parameters – dark matter.

## 1 INTRODUCTION

The standard Λcold dark matter (ΛCDM) cosmological model gives an excellent description of the growth of structure in the Universe, matching the observed temperature fluctuations in the cosmic microwave background radiation (e.g. Smoot et al. 1992; Planck Collaboration XVI 2014), the growth of large-scale structure (e.g. Springel, Frenk & White 2006), the clustering of galaxies (Crocce et al. 2016), large-scale weak lensing distortions (e.g. Blandford et al. 1991; Fu et al. 2014), baryon acoustic oscillations (e.g. Blake & Glazebrook 2003; Eisenstein et al. 2005; Dawson et al. 2013) and the flux power spectrum of quasar absorption lines (e.g. Croft et al. 1998; Baur et al. 2016). However, over the past two decades there have been persistent tensions claimed on small scales inside galaxy groups and individual galaxies. These include the following.

(i) *The 'missing satellites' problem*: pure dark matter cosmological simulations of structure formation predict that thousands of bound dark matter haloes should be orbiting the Milky Way and Andromeda, yet only a few tens of visible satellites have been observed to date (e.g. Klypin et al. 1999; Moore et al. 1999; McConnachie 2012).

(ii) *The 'cusp-core' problem*: these same simulations predict that the dark matter density distribution within galaxies should be self-similar and well fitted at the ∼10 per cent level by the 'NFW' profile (Navarro, Frenk & White 1996b):

$$\rho_{\mathrm{NFW}}(r) = \rho_0 \left(\frac{r}{r_{\mathrm{s}}}\right)^{-1} \left(1 + \frac{r}{r_{\mathrm{s}}}\right)^{-2} \quad (1)$$

where the central density $\rho_0$ and scalelength $r_{\mathrm{s}}$ are given by

$$\rho_0 = \rho_{\mathrm{crit}} \Delta c^3 g_c/3; \quad r_{\mathrm{s}} = r_{200}/c \quad (2)$$

⋆ E-mail: justin.inglis.read@gmail.com

$$g_c = \frac{1}{\log(1+c) - \frac{c}{1+c}}; \quad r_{200} = \left[\frac{3}{4} M_{200} \frac{1}{\pi \Delta \rho_{\rm crit}}\right]^{1/3}. \tag{3}$$

$c$ is the dimensionless 'concentration parameter'; $\Delta = 200$ is the over-density parameter; $\rho_{\rm crit}$ is the critical density of the Universe today; $r_{200}$ is the 'virial' radius at which the mean enclosed density is $\Delta \times \rho_{\rm crit}$; and $M_{200}$ is the 'virial' mass within $r_{200}$.

For over two decades now, the rotation curves of small dwarf and low surface brightness galaxies have favoured a central constant density core over the 'cuspy' NFW profile described above (e.g. Flores & Primack 1994; Moore 1994; de Blok & Bosma 2002; Kuzio de Naray & Kaufmann 2011; Oh et al. 2011; Hague & Wilkinson 2013).

(iii) *The 'too big to fail' (TBTF) problem*: the central velocity dispersion of Local Group dwarfs appears to be too low to be consistent with the most massive subhaloes in ΛCDM (Read et al. 2006; Boylan-Kolchin, Bullock & Kaplinghat 2011).

The above puzzles could be hinting at physics beyond ΛCDM, for example exotic inflation models (e.g. Zentner & Bullock 2002), or exotic dark matter models (e.g. Moore 1994; Rocha et al. 2013; Elbert et al. 2015). However, it is important to emphasize that all of these puzzles arise from a comparison between the observed Universe and a model ΛCDM universe entirely devoid of stars and gas (that we shall refer to from here on as 'baryons'; e.g. see the discussion in Pontzen & Governato 2014 and Read 2014). Semi-analytic models make some attempt to improve on this by painting stars on to pure dark matter simulations (e.g. Baugh 2006). However, implicit in such analyses is an assumption that the distribution of dark matter is unaltered by the process of galaxy formation. It is becoming increasingly likely that this assumption is poor, especially within group environments and on the scale of tiny dwarf galaxies.

Navarro, Eke & Frenk (1996a) were the first to suggest that dark matter could be collisionlessly heated by impulsive gas mass loss driven by supernova explosions. They found that, for reasonable initial conditions corresponding to isolated dwarf galaxies, the effect is small (see also Gnedin & Zhao 2002). However, Read & Gilmore (2005) showed that the effect can be significant if star formation proceeds in repeated bursts, gradually grinding a dark matter cusp down to a core. There is mounting observational evidence for such bursty star formation (Leaman et al. 2012; Weisz et al. 2012a; Teyssier et al. 2013; Kauffmann 2014; McQuinn et al. 2015), while the physics of such 'cusp-core transformations' is now well-understood (Pontzen & Governato 2012; Pontzen et al. 2015, and for a review see Pontzen & Governato 2014). The latest numerical simulations that resolve the effect of individual supernovae explosions are substantially more predictive (e.g. Chan et al. 2015; Oñorbe et al. 2015; Read, Agertz & Collins 2016a, hereafter R16a); these demonstrate that dark matter cores are an unavoidable prediction of ΛCDM (with baryons) for all low-mass dwarf galaxies, so long as star formation proceeds for long enough.[1]

However, there remains a debate in the literature over the efficiency of star formation in low-mass haloes. Di Cintio et al. (2014), Chan et al. (2015) and Tollet et al. (2016) find insufficient star formation to excite cusp-core transformations below $M_{200} \sim 10^{10}$ M$_\odot$; Madau, Shen & Governato (2014) find that core formation proceeds in $M_{200} \sim 10^9$ M$_\odot$ dwarfs; and R16a find that core formation proceeds 'all the way down' to halo masses $\sim 10^8$ M$_\odot$. These differences owe in part to resolution. R16a have a typical spatial resolution of 4 pc for their isolated dwarfs, with a stellar and dark matter particle mass resolution of ∼250 M$_\odot$. This allows them to resolve the $\lesssim 500$ pc size cores that form in their $M_{200} \lesssim 10^9$ M$_\odot$ dwarfs. Such small cores cannot be captured by the Di Cintio et al. (2014) and Tollet et al. (2016) simulations that have a spatial resolution of ∼ 80–100 pc. However, Chan et al. (2015) have a spatial resolution of ∼30 pc for their $10^9$ M$_\odot$ dwarf, yet they find that no significant dark matter core forms. This owes to a second key difference between these studies: the treatment of reionization. In R16a, reionization is not modelled and so star formation is allowed to proceed unhindered at very low halo mass. In all of the other studies, some model of reionization heating is included. But the mass scale at which reionization begins to suppress star formation, $M_{\rm reion}$, remains controversial. Some recent simulations favour a high $M_{\rm reion} \sim 10^{10}$ M$_\odot$ (e.g. Chan et al. 2015; Tollet et al. 2016), while others favour a much lower $M_{\rm reion} \sim 5 \times 10^8$ M$_\odot$ (Gnedin & Kaurov 2014), consistent with the assumption of no reionization in R16a. Observationally, the continuous low star formation rate of nearby dwarf irregular galaxies (dIrrs) appears to favour a low $M_{\rm reion}$ (Ricotti 2009; Weisz et al. 2012b, and see the discussion in R16a). We will discuss $M_{\rm reion}$ further in Section 6.7.

Despite the differences in $M_{\rm reion}$, all of the above studies find that when dark matter cores do form, they are of a size of approximately the projected half stellar mass radius ($R_{1/2}$). Such cores are dynamically important by construction because they alter the dark matter distribution precisely where we can hope to measure it using stellar kinematics (R16a). They also have important effects beyond just the internal structure of galaxies. Cored dwarfs are much more susceptible to tidal shocking and stripping on infall to a larger host galaxy (e.g. Read et al. 2006; Peñarrubia et al. 2010; Brooks et al. 2013). This aids in the morphological transformation of dwarfs from discs to spheroids (Mayer et al. 2001a; Łokas, Kazantzidis & Mayer 2012; Kazantzidis, Łokas & Mayer 2013), and physically reshapes the dark matter halo mass function within groups (Peñarrubia et al. 2010; Zolotov et al. 2012; Brooks et al. 2013; Wetzel et al. 2016, and see the discussion in R16a).

Using simulations of isolated dwarfs at a spatial and mass resolution of ∼4 pc and ∼250 M$_\odot$, respectively, R16a derived a new 'CORENFW' fitting function that describes cusp-core transformations in ΛCDM over the mass range $10^8 \lesssim M_{200}/{\rm M}_\odot \lesssim 10^{10}$ (see equation 6). In Read et al. (2016b) (hereafter R16b), we showed that this gives a remarkable match to the rotation curves of four isolated dIrrs, using just two free fitting parameters: $M_{200}$ and $c$ [that take on the same meaning as in equation (1) for the NFW profile]. In particular, using mock data, we demonstrated that if the data are good enough (i.e. if the dwarfs are not face-on, starbursting and/or of uncertain distance) then we are able to successfully measure both $M_{200}$ and $c$ within our quoted uncertainties.

In this paper, we apply the rotation curve fitting method described in R16b to 19 isolated dwarf irregulars (dIrrs) to measure the stellar mass–halo mass relation $M_\star$–$M_{200}|_{\rm rot}$ over the stellar mass range $5 \times 10^5 \lesssim M_\star/{\rm M}_\odot \lesssim 10^8$. We then compare this with the stellar mass–halo mass relation obtained from 'abundance matching': $M_\star$–$M_{200}|_{\rm abund}$ to arrive at a comparatively clean test of our current cosmological model.

This paper is organized as follows. In Section 2, we show how the comparison between $M_\star$–$M_{200}|_{\rm rot}$ and $M_\star$–$M_{200}|_{\rm abund}$ constitutes a rather clean cosmological probe at the edge of galaxy formation.

[1] Two recent studies have claimed that dark matter cores do not form at any mass scale (Sawala et al. 2016b; Zhu et al. 2016). However, both of these used simulations with a 'cooling floor' of $10^4$ K, meaning that they are unable to resolve the clumpy interstellar medium. Resolving this is crucial for exciting cusp-core transformations, as explained in Pontzen & Governato (2012).

In Section 3, we describe our data compilation of rotation curves, stellar masses and stellar mass functions. In Section 4, we briefly review our rotation curve fitting method that is described and tested in detail in R16b. In Section 5, we present the results from applying our rotation curve fitting method to 19 isolated dIrrs in the field (the individual fits and fitted parameters are reported in Table 2 and Appendix A). In Section 6, we discuss the implications of our results and their relation to previous works in the literature. Finally, in Section 7 we present our conclusions.

## 2 A CLEAN COSMOLOGICAL PROBE AT THE EDGE OF GALAXY FORMATION

In this paper, we test cosmological models by comparing the stellar mass–halo mass relation derived from galaxy rotation curves ($M_\star$–$M_{200}|_{\rm rot}$) with the mean stellar mass–halo mass relation derived from 'abundance matching' ($M_\star$–$M_{200}|_{\rm abund}$). The idea in itself is not new. For example, Moster et al. (2010) compare $M_\star$–$M_{200}|_{\rm abund}$ in ΛCDM with the stellar mass–halo mass relation derived from galaxy–galaxy lensing, finding good agreement. However, most studies to date have focused on the high mass end of this relation where the differences between ΛCDM and alternative cosmologies like Λ Warm Dark Matter (ΛWDM) are small (e.g. Cacciato et al. 2009; Shan et al. 2015; and see Fig. 3). More recently, Pace (2016, hereafter P16) and Katz et al. (2017) have used the baryon-influenced mass models from Di Cintio et al. (2014) to fit rotation curves and measure $M_{200}$ and $c$ for a large sample of dwarfs, comparing their results with abundance matching predictions. We will compare and contrast our analysis with these studies in Section 6. However, what is new to this paper are the following key ingredients: (i) we focus on building a particularly clean sample of rotation curves, derived in a consistent manner and with a state-of-the-art technique $^{\rm 3D}$BAROLO (Di Teodoro & Fraternali 2015; Iorio et al. 2016); (ii) we perform our comparison at $M_\star \lesssim 10^8$ M$_\odot$, maximizing the constraints on cosmological models; and (iii) we make use of a new *predictive* coreNFW profile for the dark matter distribution on these mass scales that accounts for cusp-core transformations due to stellar feedback (R16a; R16b). In the remainder of this section, we discuss in detail how our cosmological test works and why it is particularly clean.

Classical abundance matching relies on a key assumption that galaxy stellar masses are monotonically related to dark matter halo masses (Vale & Ostriker 2004). Armed with this, galaxies are mapped to dark matter haloes of the same cumulative number density, providing a statistical estimate of $M_\star$–$M_{200}|_{\rm abund}$ for a given cosmological model. Thus, by comparing this $M_\star$–$M_{200}|_{\rm abund}$ with $M_\star$–$M_{200}|_{\rm rot}$, we arrive at a comparatively clean cosmological probe of structure formation on small scales. The probe is clean because it relies only on the following theoretical ingredients.

(i) A monotonic relation between stellar mass and halo mass. We will directly test this with our measurement of $M_\star$–$M_{200}|_{\rm rot}$ in Section 5.2.

(ii) The dark matter halo mass function. This is readily calculated for a given cosmological model using cosmological simulations (e.g. Dehnen & Read 2011; Klypin, Trujillo-Gomez & Primack 2011).

(iii) A robust prediction of the internal dark matter distribution in dIrrs $\rho_{\rm dm}(r)$, for a given cosmological model. This is required in order to measure $M_{200}$ from rotation curve data to obtain $M_\star$–$M_{200}|_{\rm rot}$. In Section 5.1 we show that while our coreNFW dark matter density profile gives a significantly better fit to our sample of rotation curves than the NFW profile, we are not particularly sensitive to this choice so long as $\rho_{\rm dm} \to \rho_{\rm NFW}$ (see equation 1) for $r > R_{1/2}$.

**Table 1.** Cosmological parameters assumed in this work. From top to bottom, these are: the Hubble parameter, the ratio of matter and dark energy density to the critical density, the 'tilt' of the power spectrum, and the amplitude of the power spectrum on a scale of $8h^{-1}$ Mpc (see e.g. Peacock 1999, for a full definition of these). These parameters are chosen to match those used in the Bolshoi simulation (Klypin et al. 2011) and give a good description of the latest cosmological data (see the discussion in Klypin et al. 2011).

| Cosmological parameter | Value |
|---|---|
| Hubble $h$ | 0.7 |
| $\Omega_{\rm M}$ | 0.27 |
| $\Omega_\Lambda$ | 0.73 |
| Tilt $n$ | 0.95 |
| $\sigma_8$ | 0.82 |

Armed with the above theory ingredients, our probe relies solely on observational data: rotation curves for dwarf galaxies with well-measured inclination and distance, and no evidence of a recent starburst (see R16b); stellar masses derived from SED model fitting[2]; and a good measure of the stellar mass function of galaxies.

For our abundance matching, we use as default the stellar mass function from Sloan Digital Sky Survey (SDSS) that reaches down to $M_\star \sim 10^7$ M$_\odot$ (Blanton et al. 2005; Baldry, Glazebrook & Driver 2008; Behroozi, Conroy & Wechsler 2010; Behroozi, Wechsler & Conroy 2013) and the halo mass function from the ΛCDM 'Bolshoi' simulation that is accurate to $M_{200} \sim 10^{10}$ M$_\odot$ (Klypin et al. 2011; the cosmological parameters assumed by this simulation are reported in Table 1). Below these mass scales, we use power-law extrapolations. We compare the SDSS stellar mass function to those derived in Read & Trentham (2005) (hereafter RT05), GAMA (Baldry et al. 2012) and zCOSMOS (Giodini et al. 2012) in Fig. 1. The survey data are described in Section 3.2, while we explore reasons for their different faint end slopes in Section 5.3.

In addition to testing a ΛCDM cosmology, we explore an effective Λ 'warm' dark matter cosmology (ΛWDM). This corresponds to a dark matter particle that is relativistic for some time after decoupling in the early Universe, leading to a suppression in the growth of structure on small scales and at early times (e.g. Avila-Reese et al. 2001; Bode, Ostriker & Turok 2001). We describe this model in detail in Section 5.5.

## 3 THE DATA

### 3.1 The rotation curve sample

We compile H I data for 19 isolated dIrrs over the mass range $5 \times 10^5 \lesssim M_\star/{\rm M}_\odot \lesssim 10^8$ from Weldrake, de Blok & Walter (2003) and Oh et al. (2015), and stellar mass and surface density data from Zhang et al. (2012). Our sample selection, which primarily comprises a subset of Little THINGS galaxies, is discussed in detail in Iorio et al. (2016) and R16b. We exclude galaxies that are known to have very

[2] Note that such stellar masses are theoretically derived quantities, not directly measured from the data. However, this critique applies equally to the stellar masses derived for $M_\star$–$M_{200}|_{\rm rot}$ and $M_\star$–$M_{200}|_{\rm abund}$. As such, the *comparison* between these two should not be sensitive to the details of our stellar mass modelling, so long as we are consistent.

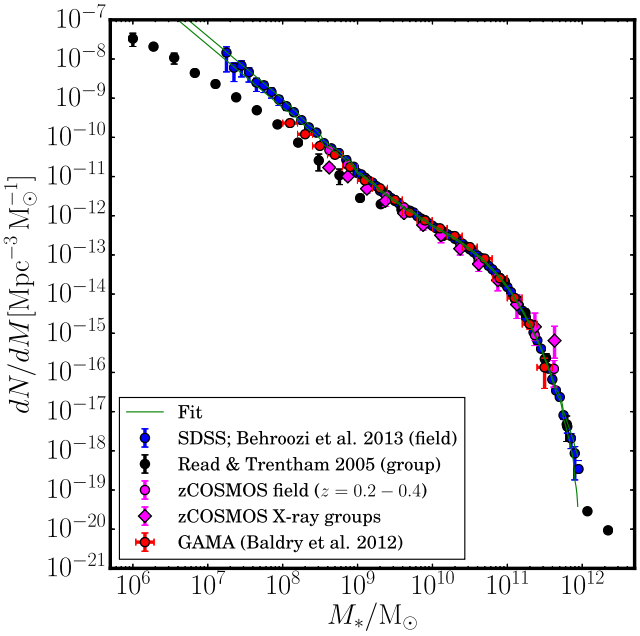


**Figure 1.** Galaxy stellar mass functions compiled from the literature. The blue data points show the stellar mass function from SDSS (Behroozi et al. 2013), the black data points show the group stellar mass function from RT05, the red data points show the stellar mass function from GAMA (Baldry et al. 2012) and the magenta data points show the stellar mass functions from zCOSMOS field galaxies over the redshift range $z$=0.2–0.4 (circles) and from X-ray selected groups (diamonds; Giodini et al. 2012 and see Section 3 for further details). The green tracks show a non-parametric fit to the SDSS stellar mass function, where the upper and lower tracks encompass the 68 per cent confidence intervals of the data. Below $M_\star = 10^8$ M$_\odot$ we assume a power law with logarithmic slope $\alpha = 1.6$.

low inclination (for which the rotation curve extraction can become biased; R16b), four Blue Compact Dwarfs and any galaxy for which there is no published stellar mass profile. This leaves about half of the full Little THINGS sample. Iorio et al. (2016) show that this subset is representative of the full Little THINGS survey in terms of its distribution of distances, absolute magnitudes, star formation rate densities and baryonic masses.

In addition, we include two galaxies which do not have gaseous rotation curves: the isolated dwarf irregular Leo T and the Milky Way dwarf spheroidal galaxy Carina. We estimate $M_{200}$ for Leo T by direct comparison to the simulations in R16a. There, we showed that Leo T gave a poor match to our $M_{200} = 10^8$ M$_\odot$ and $M_{200} = 10^9$ M$_\odot$ simulations, but an excellent match to the photometric light profile, star formation history, stellar metallicity distribution function and star/gas kinematics of our $M_{200} = 5 \times 10^8$ M$_\odot$ simulation. From this comparison, we estimate $M_{200,\,\mathrm{LeoT}} = 3.5 - 7.5 \times 10^8$ M$_\odot$ (see Table 2). (A similar analysis for the Aquarius dwarf yields a mass $M_{200} \sim 10^9$ M$_\odot$ in good agreement with its rotation curve derived value; see Table 2.) For Carina, we use the pre-infall 'tidal mass estimate' from Ural et al. (2015). This is derived by directly fitting $N$-body simulations of Carina tidally disrupting in the halo of the Milky Way to data for the positions and velocities of 'extra-tidal' stars reported in Muñoz et al. (2006). Leo T is interesting because it is the lowest mass dwarf discovered to date with ongoing star formation (Ryan-Weber et al. 2008). In R16a, we argued that its lack of a visible H I rotation curve owes to it having a low inclination ($i < 20^\circ$). Carina is interesting because, despite its close proximity to the Milky Way, it has continued to form stars for almost a Hubble time (though with notable bursts; de Boer et al. 2014). We use Carina to discuss at what mean orbital distance from the Milky Way environmental effects start to play an important role, driving scatter in the $M_\star$–$M_{200}|_{\mathrm{rot}}$ relation (Section 6).

All of the data are summarized in Table 2, including our derived model fitting parameters. We describe our methodology for extracting the rotation curves from the H I data cubes and fitting model rotation curves in Section 4.

### 3.2 The stellar mass functions

We take the SDSS stellar mass function from Behroozi et al. (2013), which was originally obtained by Baldry et al. (2008). The uncertainty on the stellar mass is comparable to our assumed uncertainty for the isolated dwarf galaxy sample described above of ∼25 per cent (Oh et al. 2015), making the comparison between the stellar masses in Behroozi et al. (2013) and those taken from Zhang et al. (2012) entirely reasonable.

In Fig. 1, we compare the SDSS stellar mass function (blue data points) with those derived by RT05 (black data points; hereafter RT05); GAMA (red data points; Baldry et al. 2012) and zCOSMOS (magenta data points; Giodini et al. 2012).

The SDSS stellar mass function is derived from the Blanton et al. (2005) survey of low-luminosity galaxies (Baldry et al. 2008). This is complete to a stellar mass of $M_\star \sim 2 \times 10^7$ M$_\odot$ over a volume of $\sim 2 \times 10^6$ Mpc$^3$. The GAMA stellar mass function is derived from about a tenth of the SDSS survey volume ($\sim 2 \times 10^5$ Mpc$^3$), and is complete to a stellar mass of $M_\star \sim 10^8$ M$_\odot$. Due to its smaller survey volume, its stellar mass function is more prone to cosmic variance (Blanton et al. 2005; Driver et al. 2011). The zCOSMOS survey covers a small 1.7 deg$^2$ patch of the sky, but to much higher redshift (Lilly et al. 2007). Here, we use the lowest redshift range $0.2 < z < 0.4$ that corresponds to a volume similar to that of the GAMA survey ($\sim 1.8 \times 10^5$ Mpc$^3$), complete down to a stellar mass of $M_\star \sim 4 \times 10^8$ M$_\odot$ (Giodini et al. 2012). The full zCOSMOS sample is split into a 'field' population (magenta circles) and X-ray selected groups (magenta diamonds), both over the redshift range $0.2 < z < 0.4$. Since group environments are more dense on average, we renormalize the X-ray selected groups from Giodini et al. (2012) to match SDSS at $M_\star = 10^{10}$ M$_\odot$. Finally, we consider the stellar mass function from RT05. At $M_\star \gtrsim 10^9$ M$_\odot$, this is taken from SDSS (Blanton et al. 2001, 2003); at lower stellar mass it comes from the Trentham & Tully (2002) catalogue of five nearby groups, including the Local Group (see Trentham, Sampson & Banerji 2005 for details of how these surveys are sewn together). The Trentham & Tully (2002) group catalogue is derived from deep mosaic surveys that are complete to a stellar mass of $M_\star \sim 10^6$ M$_\odot$, but cover a tiny volume as compared to SDSS of just ∼5 Mpc$^3$.

As can be seen in Fig. 1, all of these different stellar mass functions agree within their uncertainties above $M_\star \sim 10^9$ M$_\odot$. However, at lower stellar masses there is a striking divergence between all of them bar SDSS and the zCOSMOS field stellar mass function that are in good agreement. We discuss this further, and the possible reasons for it, in Section 5.3.

## 4 EXTRACTING AND MODELLING DWARF GALAXY ROTATION CURVES

### 4.1 Extracting rotation curves from H I data cubes

Our rotation curves are derived from H I data cubes (Weldrake et al. 2003; Oh et al. 2015) using the publicly available software

**Table 2.** Data and derived rotation curve fitting parameters for 19 isolated dIrrs and two Milky Way satellite dwarfs. The dIrrs are divided into a clean sample, inclination 'rogues', disequilibrium rogues and distance rogues, as marked (see section 4.4 for more details). We highlight galaxies with high gas fractions $M_{\rm gas}/M_\star > 20$ with a '•'. Column 1 gives the galaxy name. Columns 2–7 give the data for that galaxy: the peak asymmetric drift corrected rotation curve velocity $v_{\rm max}$; the distance to the galaxy $D$; the stellar mass, with errors $M_\star$; the total gas mass $M_{\rm gas}$; and the exponential stellar and gas disc scalelengths $R_\star$ and $R_{\rm g}$, respectively. Column 8 gives the radial range used in the fit to the rotation curve $[R_{\rm min}, R_{\rm max}]$ ('–' indicates that $R_{\rm max}$ is set to the outermost data point). Columns 9–10 give the marginalized dark matter halo parameters: the virial mass $M_{200}$ and concentration parameter $c$, with 68 per cent confidence intervals. Column 11 gives the reduced $\chi^2_{\rm red}$ of the fit. Column 12 reports data on the presence of H I bubbles that can indicate disequilibria (see R16b). The size and expansion velocity of the largest bubble are given ('–' denotes no reported measurement). Finally, Column 12 gives the data references for that galaxy, as follows: 1: Barnard (1884); 2: Weldrake et al. (2003); 3: Zhang et al. (2012); 4: Górski, Pietrzyński & Gieren (2011); 5: Leaman et al. (2012); 6: Oh et al. (2015); 7: de Blok & Walter (2000); 8: Kepley et al. (2007); 9: Silich et al. (2006); 10: van Eymeren et al. (2009); 11: Warren et al. (2011); 12: Ashley, Simpson & Elmegreen (2013); 13: Puche et al. (1992); 14: Johnson et al. (2012); 15: Ural et al. (2015); 16: Martin, de Jong & Rix (2008); 17: Weisz et al. (2012b); 18: Ryan-Weber et al. (2008); 19: Kirby et al. (2013b); 20: R16a; 21: Irwin & Hatzidimitriou (1995); 22: de Boer et al. (2014); 23: Makarova (1999). The last two rows show data for the isolated dwarf irregular Leo T and the Milky Way dwarf spheroidal galaxy Carina, neither of which have gaseous rotation curves. We estimate $M_{200}$ for Leo T by direct comparison to the simulations in R16a (see Section 3); for Carina, we use the pre-infall 'tidal mass estimate' from Ural et al. (2015).

| Galaxy | $v_{\rm max}$ (km s$^{-1}$) | $i$ (°) | $D$ (Mpc) | $M_\star$ ($10^7$ M$_\odot$) | $M_{\rm gas}$ ($10^7$ M$_\odot$) | $R_\star$ (kpc) | $R_{\rm gas}$ (kpc) | $[R_{\rm min}, R_{\rm max}]$ (kpc) | $M_{200}$ ($10^{10}$ M$_\odot$) | $c$ | $\chi^2_{\rm red}$ | H I bubbles | Refs. |
|---|---|---|---|---|---|---|---|---|---|---|---|---|---|
| NGC 6822 | $56.0 \pm 2.2$ | 65–75 | $0.49 \pm 0.04$ | $7.63 \pm 1.9$ | 17.4 | 0.68 | 1.94 | [2.5, –] | $2^{+0.2}_{-0.3}$ | $15.1^{+1.8}_{-0.8}$ | 0.37 | 1.4 – 2 kpc; 0 km s$^{-1}$ | 1,2,3,7 |
| WLM | $39.0 \pm 3.3$ | $74 \pm 2.3$ | $0.985 \pm 0.033$ | $1.62 \pm 0.4$ | 7.9 | 0.75 | 1.04 | [0, –] | $0.83^{0.2}_{-0.2}$ | $17^{+3.9}_{-2.2}$ | 0.27 | 0.46 kpc; 0 km s$^{-1}$ | 3,4,5,6,8 |
| DDO 52 | $50.7 \pm 13.4$ | $55.1 \pm 2.9$ | 10.3 | $5.27 \pm 1.3$ | 37.1 | 0.94 | 2.49 | [0, –] | $1.2^{+0.29}_{-0.27}$ | $17.3^{+4.2}_{-2.4}$ | 0.2 | – | 3,6 |
| 11 DDO 87 | $52.0 \pm 9.1$ | $42.7 \pm 7.3$ | 7.4 | $3.3 \pm 0.8$ | 31.0 | 1.13 | 1.51 | [0, –] | $1.13^{+0.27}_{-0.25}$ | $17.6^{+4.6}_{-2.7}$ | 0.31 | – | 3,6 |
| DDO 154• | $46.7 \pm 5.1$ | $67.9 \pm 1.1$ | 3.7 | $0.835 \pm 0.2$ | 30.9 | 0.54 | 2.34 | [0, –] | $1.26^{+0.05}_{-0.05}$ | $14.2^{+0.24}_{-0.17}$ | 2.14 | – | 3,6 |
| DDO 210 | $17.8 \pm 9.5$ | $63.2 \pm 3.2$ | 0.9 | $0.068 \pm 0.017$ | 0.33 | 0.22 | 0.25 | [0.2, –] | $0.068^{+0.13}_{-0.04}$ | $21.4^{+5.5}_{-5.2}$ | 0.65 | – | 3,6 |
| NGC 2366 | $58.8 \pm 5.4$ | $65.1 \pm 4.2$ | 3.4 | $6.95 \pm 1.73$ | 103 | 1.54 | 2.69 | [0, –] | $2.4^{+0.49}_{-0.54}$ | $17.3^{+4.5}_{-2.4}$ | 0.48 | 0.5 – 1 kpc; 30 km s$^{-1}$ | 3,6,10 |
| UGC 8508 | $32.1 \pm 6.2$ | $67.6 \pm 5.3$ | 2.6 | $0.764 \pm 0.191$ | 3.5 | 0.31 | 1.1 | [0, –] | $0.63^{+0.5}_{-0.2}$ | $21.0^{+5.3}_{-4.8}$ | 0.05 | 0.285 pc; 0 km s$^{-1}$ | 3,6,11 |
| CVnIdwA | $22.4 \pm 3.9$ | $49.2 \pm 10.9$ | 3.6 | $0.41 \pm 0.1$ | 6.42 | 0.68 | 1.18 | [0, –] | $0.17^{+0.1}_{-0.05}$ | $21.4^{+5.4}_{-5.3}$ | 0.21 | – | 3,6 |
| DDO 126 | $39.2 \pm 3.1$ | $62.2 \pm 2.9$ | 4.9 | $1.61 \pm 0.4$ | 18.7 | 0.82 | 1.51 | [2, –] | $0.58^{+0.2}_{-0.1}$ | $20.6^{+5.9}_{-4.7}$ | 0.16 | – | 3,6 |
| DDO 168 | $56.3 \pm 7.2$ | $47.3 \pm 7.4$ | 4.3 | $5.9 \pm 1.48$ | 45.8 | 0.82 | 1.51 | [0, –] | $2.1^{+0.52}_{-0.48}$ | $16.8^{+3.2}_{-2.0}$ | 0.24 | – | 3,6 |
| ——— *i*-Rogues ——— | | | | | | | | | | | | | |
| DDO 133 | $49.0 \pm 5.1$ | $36.9^{+2.3}_{-4.0}$ | 3.5 | $3.04 \pm 0.76$ | 16.9 | 0.804 | 1.39 | [0, –] | $1.6^{+1.1}_{-0.44}$ | $25.8^{+2.8}_{-5.5}$ | 0.16 | – | 3,6 |
| IC 1613 | $19.9 \pm 2.2$ | $27.6^{+9.0}_{-11.3}$ | $0.74 \pm 0.01$ | $1.5 \pm 0.5$ | 8 | 0.65 | 1.29 | [1.9, –] | $0.17^{+1.0}_{-0.1}$ | $21.8^{+5.3}_{-5.4}$ | 0.13 | 1 kpc; 25 km s$^{-1}$ | 3,6,9 |
| DDO 50 | $37.6 \pm 10.1$ | $37.4^{+2.0}_{-3.7}$ | 3.4 | $10.72 \pm 2.68$ | 97.65 | 0.89 | 3.1 | [0, –] | $0.32^{+0.16}_{-0.08}$ | $26.2^{+2.5}_{-4.7}$ | 0.8 | 0.65-0.84 kpc; 14 km s$^{-1}$ | 3,6,13 |
| DDO 53• | $23.2 \pm 6.6$ | $23.9^{+7.3}_{-6.4}$ | 3.6 | $0.97 \pm 0.24$ | 24.6 | 0.89 | 1.14 | [0, –] | $0.39^{+3.4}_{-0.36}$ | $21.6^{+5.3}_{-5.1}$ | 0.38 | – | 3,6 |
| DDO 47 | $62.6 \pm 5.2$ | $31.4^{+5.7}_{-5.2}$ | 5.2 | $9.4 \pm 4.7$ | 35.3 | 0.7 | 8.2 | [3.5, –] | $4.4^{+3.2}_{-1.9}$ | $20.5^{+5.6}_{-4.6}$ | 0.83 | – | 6,23 |
| ——— Disequilibrium rogues ——— | | | | | | | | | | | | | |
| DDO 216 | $13.8 \pm 5.0$ | $70.0 \pm 5.0$ | 1.1 | $1.52 \pm 0.38$ | 0.152 | 0.52 | 0.297 | [0, –] | $0.067^{+0.048}_{-0.025}$ | $23.4^{+4.6}_{-6.0}$ | 0.52 | – | 3,6 |
| NGC 1569 | $55.9 \pm 22.4$ | $67.0 \pm 5.6$ | 3.4 | $36 \pm 9$ | 23.8 | 0.45 | 1.22 | [1.8, –] | $0.81^{+2.1}_{-0.7}$ | $19.7^{+6.7}_{-6.1}$ | – | ∼200 pc; 10-70 km s$^{-1}$ | 3,6,14 |
| ——— Distance rogues ——— | | | | | | | | | | | | | |
| DDO 101 | $64.8 \pm 2.6$ | $52.4 \pm 1.7$ | 6.4 | $6.54 \pm 1$ | 3.48 | 0.58 | 1.01 | [0, –] | $5.2^{+0.6}_{-0.4}$ | $28.9^{+0.6}_{-1.3}$ | 7.2 | – | 3,6 |
| | | | 12.9 | $26.6 \pm 4$ | 14.13 | 1.16 | 2.03 | [0, –] | $3.0^{+0.4}_{-0.2}$ | $28.3^{+1.1}_{-2.2}$ | 1.92 | – | – |
| ——— No rotation curve ——— | | | | | | | | | | | | | |
| Leo T | – | ∼20° | $0.407 \pm 0.038$ | $0.0135 \pm 0.008$ | 0.028 | 0.106 | – | – | 0.035 – 0.075 | – | – | – | 16,17,18,19,20 |
| Carina | – | – | $0.085 \pm 0.005$ | $0.048^{+0.006}_{-0.004}$ | – | 0.177 | – | – | $0.036^{+0.038}_{-0.023}$ | – | – | – | 15,21,22 |

$^{3D}$BAROLO (Di Teodoro & Fraternali 2015). $^{3D}$BAROLO fits tilted-ring models directly to the data cube by building artificial 3D data and minimizing the residuals, without explicitly extracting velocity fields (as in e.g. Oh et al. 2015). This ensures full control of the observational effects and, in particular, a proper account of beam smearing that can strongly affect the derivation of the rotation velocities in the inner regions of dwarf galaxies (see e.g. Swaters 1999). $^{3D}$BAROLO was extensively tested on mock data in R16b and shown to give an excellent recovery of the rotation curve so long as the best-fitting inclination angle was $i_{\rm fit} > 40^\circ$. The final rotation curves were corrected for asymmetric drift, as described in R16b and Iorio et al. (2016). The detailed description of the data analysis, including comments on individual galaxies, are presented in those papers.

### 4.2 The mass model

We use the same mass model as described in detail in R16b. Briefly, we decompose the circular speed curve into contributions from stars, gas and dark matter:

$$v_c^2 = v_*^2 + v_{\rm gas}^2 + v_{\rm dm}^2, \tag{4}$$

where $v_\star$ and $v_{\rm gas}$ are the contributions from stars and gas, respectively, and $v_{\rm dm}$ is the dark matter contribution. We assume that both the stars and gas are well-represented by exponential discs:

$$v_{*/\rm gas}^2 = \frac{2\,G M_{*/\rm gas}}{R_{*/\rm gas}} y^2 \left[I_0(y)K_0(y) - I_1(y)K_1(y)\right] \tag{5}$$

where $M_{\star/\rm gas}$ is the mass of the star/gas disc, respectively; $R_{\star/\rm gas}$ is the exponential scalelength; $y = R/M_{\star/\rm gas}$ is a dimensionless radius parameter; and $I_0, I_1, K_0$ and $K_1$ are Bessel functions (Binney & Tremaine 2008). We fix the values of $R_\star$ and $R_{\rm gas}$ in advance of running our Markov Chain Monte Carlo (MCMC) models (see Section 4.3). All values used are reported in Table 2.

For the dark matter profile, we use the coreNFW profile from R16a:

$$M_{\rm cNFW}(< r) = M_{\rm NFW}(< r) f^n \tag{6}$$

where $M_{\rm NFW}(< r)$ is the usual NFW enclosed mass profile (Navarro et al. 1996b):

$$M_{\rm NFW}(< r) = M_{200} g_c \left[\ln\left(1 + \frac{r}{r_{\rm s}}\right) - \frac{r}{r_{\rm s}}\left(1 + \frac{r}{r_{\rm s}}\right)^{-1}\right] \tag{7}$$

and $M_{200}$, $c$, $r_{\rm s}$, $g_c$, $\rho_{\rm crit}$ and $\Delta = 200$ are as in equation (1).

The function $f^n$ generates a shallower profile below a core radius $r_{\rm c}$:

$$f^n = \left[\tanh\left(\frac{r}{r_{\rm c}}\right)\right]^n \tag{8}$$

where the parameter $0 < n \leq 1$ controls how shallow the core becomes ($n = 0$ corresponds to no core; $n = 1$ to complete core formation). The parameter $n$ is tied to the total star formation time[3] $t_{\rm SF}$:

$$n = \tanh(q); \quad q = \kappa \frac{t_{\rm SF}}{t_{\rm dyn}} \tag{9}$$

[3] More precisely, the total *duration* of star formation, not to be confused with the star formation depletion time-scale $t_{\rm dep} = \Sigma_{\rm gas}/\Sigma_{\rm SFR}$ (e.g. Bigiel et al. 2011).

where $t_{\rm dyn}$ is the circular orbit time at the NFW profile scale radius $r_{\rm s}$:

$$t_{\rm dyn} = 2\pi\sqrt{\frac{r_{\rm s}^3}{G M_{\rm NFW}(r_{\rm s})}} \tag{10}$$

and $\kappa = 0.04$ is a fitting parameter (see R16a). For the isolated dwarfs that we consider here, we assume $t_{\rm SF} = 14$ Gyr such that they have formed stars continuously for a Hubble time. For this value of $t_{\rm SF}$, $n \sim 1$ and we expect the dwarfs to be maximally cored.

The core size is set by the projected half stellar mass radius of the stars $R_{1/2}$:

$$r_{\rm c} = \eta R_{1/2} \tag{11}$$

where, for an exponential disc, $R_{1/2} = 1.68 R_\star$. By default, we assume that the dimensionless core size parameter $\eta = 1.75$, since this gives the best match to the simulations in R16a. However, as discussed in R16a, there could be some scatter in $\eta$ due to varying halo spin, concentration parameter and/or halo assembly history. We explore our sensitivity to $\eta$ in Appendix B where we perform our rotation curve fits using a flat prior on $\eta$ over the range $0 < \eta < 2.75$ (the upper bound on the $\eta$ prior is set by energetic arguments; see Appendix B for details). This allows both no core ($\eta = 0$), corresponding to an NFW profile, and substantially larger cores than were found in the R16a simulations. In Appendix B, we show that the NFW profile ($\eta = 0$) is disfavoured at >99 per cent confidence, reaffirming the well-known cusp-core problem (see Section 1). However, as we showed for WLM in R16b, $\eta$ is otherwise poorly constrained (though consistent with our default choice of $\eta = 1.75$). Allowing $\eta$ to vary slightly increases our errors on $M_{200}$ but is otherwise benign. This is because $M_{200}$ is set by the outermost bins of the rotation curve where in many cases it begins to turn over and become flat. Indeed, in Section 5.1, we show that demanding an NFW profile leads to a poor rotation curve fit, but little change in our derived halo masses. This demonstrates that so long as the dark matter density profile $\rho_{\rm dm}$ approaches the NFW form for $r > R_{1/2}$, our measurements of $M_{200}$ are not sensitive to our particular coreNFW parametrization of $\rho_{\rm dm}$.

### 4.3 Fitting the mass model to data and our choice of priors

We fit the above mass model to the data using the emcee affine invariant MCMC sampler from Foreman-Mackey et al. (2013). We assume uncorrelated Gaussian errors such that the Likelihood function is given by $\mathcal{L} = \exp(-\chi^2/2)$. We use 100 walkers, each generating 1500 models and we throw out the first half of these as a conservative 'burn in' criteria. We explicitly checked that our results are converged by running more models and examining walker convergence. All parameters were held fixed except for the dark matter virial mass $M_{200}$, the concentration parameter $c$, and the total stellar mass $M_\star$. We assume a flat logarithmic prior on $M_{200}$ of $8 < \log_{10}[M_{200}/{\rm M}_\odot] < 11$, a flat linear prior on $c$ of $14 < c < 30$ and a flat linear prior on $M_\star$ over the range given by stellar population synthesis modelling, as reported in Table 2. For the mock simulation data and the real data, we assume an error on $M_\star$ of 25 per cent unless a larger error than this is reported in the literature (Zhang et al. 2012; Oh et al. 2015). The generous prior range on $c$ is set by the cosmic mean redshift $z = 0$ expectation value of $c$ at the extremities of the prior on $M_{200}$ (Macciò et al. 2007). In R16b, we showed that our results are not sensitive to this prior choice. For each galaxy, we fit data over a range $[R_{\rm min}, R_{\rm max}]$ as reported in Table 2, where '–' means that $R_{\rm max}$ was set by the outermost data

point. $R_{\rm min}$ is marked by thin vertical lines on the individual rotation curve fits reported in Appendix A. For most galaxies, $R_{\rm min} = 0$. It is only non-zero where the innermost rotation curve is affected by an expanding H I bubble (see R16b for further details). In Appendix B, we explore allowing the core size parameter $\eta$ (equation 11) to vary also in the fits.

### 4.4 Tests on mock data and the exclusion of 'rogues'

Our ability to measure $M_{200}$ and $c$ from mock rotation curve data was extensively tested in R16b. There, we showed that there are three key difficulties that can lead to systematic biases. First, we must account for cusp-core transformations due to stellar feedback if we wish to obtain a good fit to the rotation curve inside $R_{1/2}$. We account for this by using our coreNFW profile (Section 4.2). Secondly, our simulated dwarfs continuously cycle between quiescent and 'starburst' modes that cause the H I rotation curve to fluctuate. This can lead to a systematic bias on $M_{200}$ of up to half a dex in the most extreme cases. However, this disequilibrium can be readily identified by the presence of large and fast-expanding ($\gtrsim$ 20–30 km s$^{-1}$) H I superbubbles in the ISM. Thirdly, low inclination galaxies, particularly if also undergoing a starburst, can be difficult to properly inclination correct. Using mock H I data cubes, we found that $^{\rm 3D}$BAROLO can return a systematically low inclination if $i_{\rm fit} \lesssim 40^\circ$. For this reason, if $^{\rm 3D}$BAROLO returns an inclination of $i_{\rm fit} < 40^\circ$, we marginalize over $i$ in our fits assuming a flat prior over the range $0^\circ < i < 40^\circ$. We call such galaxies 'inclination Rogues' or $i$-Rogues and we discuss them in Appendix B. (We find that five of our 19 dIrrs are $i$-Rogues.)

Two galaxies – DDO 216 (Pegasus) and NGC 1569 – have highly irregular rotation curves. For Pegasus, this owes to the limited radial extent of its rotation curve that does not extend beyond $R_{1/2}$. For NGC 1569, its inner rotation curve is shallower than required to support even its stellar mass, indicating that it is far from equilibrium. This is further supported by the presence of large and fast-expanding H I holes (see R16b, Table 2 and Johnson et al. 2012) and the fact that it is classified as a 'Blue Compact Dwarf', with a very recent starburst some ∼40 Myr ago (McQuinn et al. 2010). [Indeed, Lelli, Verheijen & Fraternali (2014) classify it as having a 'kinematically disturbed H I disc' and do not attempt to derive its rotation curve.] From a more theoretical standpoint, R16b and more recently El-Badry et al. (2017) show that starbursts are expected to drive exactly the sort of disequilibrium seen in NGC 1569. For these reasons, we exclude these two 'disequilibrium rogues' from further analysis from here on. For completeness, we report their best-fitting $M_{200}$ and $c$ in Table 2 and we show their rotation curve fits in Appendix A.

Finally, one galaxy – DDO 101 – has a very uncertain distance; we refer to this galaxy as a 'distance Rogue'. We discussed DDO 101 in detail in R16b, showing that for a distance of ∼12 Mpc it can be well fitted by a coreNFW dark matter halo. We consider its position on the $M_\star$–$M_{200}|_{\rm rot}$ relation alongside the $i$-Rogues in Appendix B.

## 5 RESULTS

### 5.1 The rotation curve fits

In Fig. 2, we show three example rotation curve fits for CVnIdwA, WLM and NGC 6822, chosen to span the range of stellar masses in our full sample (see Table 2). (We show the full sample, including the 'rogues', in Appendix A.) The black contours show the median (black), 68 per cent (dark grey) and 95 per cent (light grey) confidence intervals of our fitted rotation curve models (see Section 4.2). The vertical green dashed line shows the projected stellar half light radius $R_{1/2}$. The thin vertical black line marks the inner data point used for the fit, $R_{\rm min}$ (where this is not marked $R_{\rm min} = 0$). The blue and green lines show the rotation curve contribution from stars and gas, respectively. The top three panels of Fig. 2 show fits using the coreNFW profile, the bottom three using an NFW profile, where we set $R_{\rm min}$ to ensure that the outer rotation curve is well fitted (see Section 4 for details of our fitting methodology and priors).

As can be seen in Fig. 2, in all three cases the coreNFW profile provides an excellent fit to the data, while the NFW profile gives a poor fit, reaffirming the longstanding 'cusp-core' problem (see Section 1). The good fits that we find when using the coreNFW profile are particularly striking since, like the NFW profile, it has only two free parameters: $M_{200}$ and $c$ (see Section 4.2). However, despite the NFW profile giving a poor fit to the rotation curve shape, the NFW-derived $M_{200}$ are actually in good agreement with those from our coreNFW fits. For NGC 6822, we find $M_{200,\rm NFW} = 2.0^{+0.13}_{-0.2} \times 10^{10}$ M$_\odot$; for WLM, $M_{200,\rm NFW} = 5.2^{+2.1}_{-1.2} \times 10^9$ M$_\odot$; and for CVnIdwA, $M_{200,\rm NFW} = 0.79^{+0.5}_{-0.3} \times 10^9$ M$_\odot$. These agree, within our 68 per cent confidence intervals, with the coreNFW values reported in Table 2.

The above demonstrates that the coreNFW profile is important for obtaining a good fit to the rotation curve shape inside $\sim R_{1/2}$; however it is not critical for measuring $M_{200}$. What matters for measuring $M_{200}$ is that the dark matter density profile approaches the NFW form for $r > R_{1/2}$ (as is the case for the coreNFW profile by construction). Since there is not enough integrated supernova energy to unbind the dark matter cusp on scales substantially larger than $R_{1/2}$ (see e.g. Peñarrubia et al. 2012; R16a and Section 6), this demonstrates that our results for $M_{200}$ are robust to the details of stellar feedback-induced dark matter heating. We confirm this in Appendix B, where we show that allowing the dark matter core size to vary freely in the fits slightly inflates the errors on $M_{200}$, but does not otherwise affect our results.

### 5.2 The stellar mass–halo mass relation of isolated field dwarfs

In Fig. 3, we plot the stellar mass–halo mass relation of the 11 'clean' isolated dIrrs listed in Table 2, as derived from their H I rotation curves (see Section 4). For our 'clean' sample, we include all galaxies with inclination $i_{\rm fit} > 40^\circ$, well-measured distance and no obvious signs of disequilibrium (see Section 4.4). The individual rotation curves for these galaxies are reported in Appendix A. There, we also show the rotation curves for the 'rogues' that did not make the above cut (see Table 2). In addition, in Fig. 3 we plot two galaxies that do not have H I rotation curves: the isolated dwarf irregular Leo T (red diamond) and the Milky Way dwarf spheroidal galaxy Carina (black triangle). We estimate $M_{200}$ for Leo T by direct comparison to the simulations in R16a (see Section 3 and Table 2); for Carina, we use the pre-infall 'tidal mass estimate' from Ural et al. (2015). We discuss Carina further in Section 6.5. Overplotted in Fig. 3 are $M_\star$–$M_{200}|_{\rm abund}$ calculated from abundance matching in ΛCDM using the SDSS field stellar mass function (solid blue lines) and the RT05 stellar mass function of nearby groups (red shaded region). We discuss these in Section 5.4.

Notice from Fig. 3 that the isolated dwarfs show remarkably little scatter, defining a monotonic line in $M_\star$–$M_{200}|_{\rm rot}$ space within their 68 per cent confidence intervals. Such monotonicity is a key assumption of abundance matching and Fig. 3 demonstrates that this assumption is empirically justified, at least for the sample

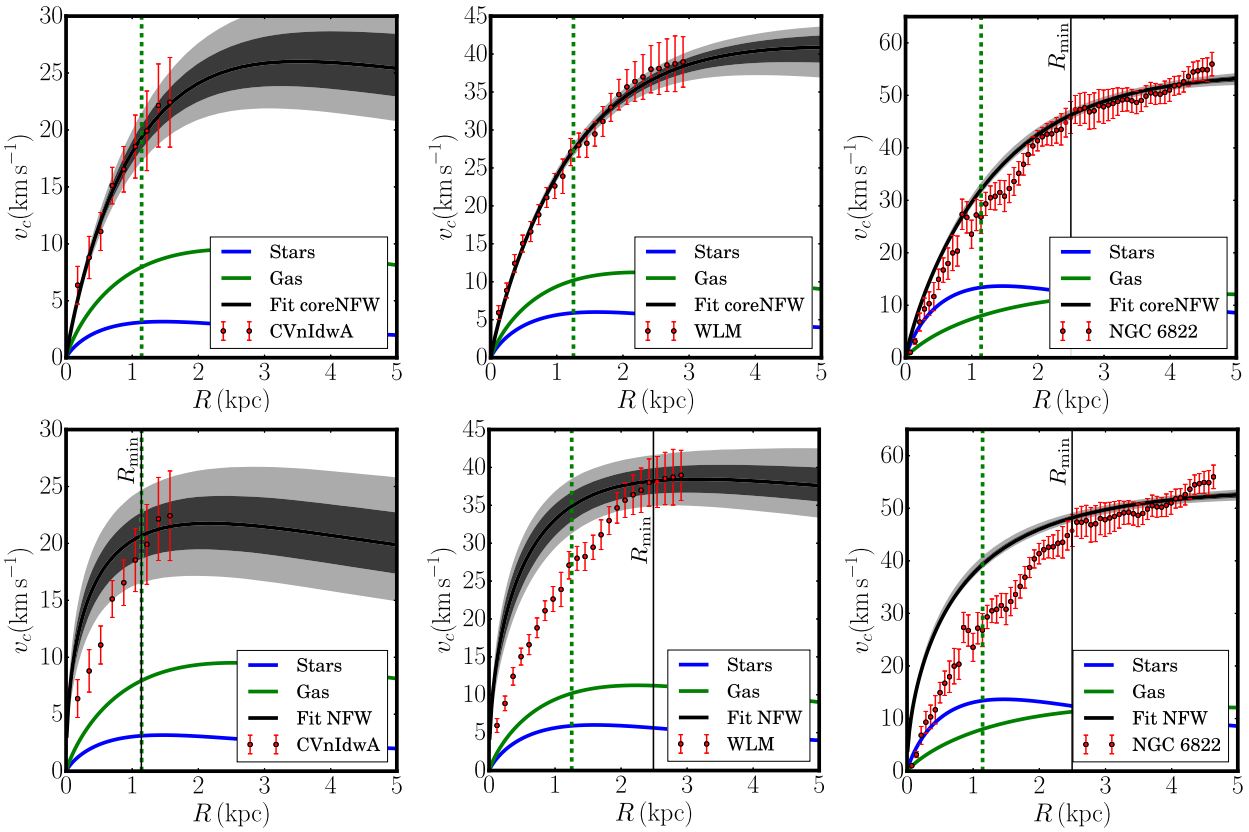


**Figure 2.** Rotation curve fits for three example galaxies: CVnIdwA, WLM and NGC 6822, chosen to span the range of stellar masses in our full sample (see Table 2). We show the full sample, including the 'rogues', in Appendix A. The black contours show the median (black), 68 per cent (dark grey) and 95 per cent (light grey) confidence intervals of our fitted rotation curve models (see Section 4.2). The vertical green dashed line shows the projected stellar half light radius $R_{1/2}$. The thin vertical black line marks the inner data point used for the fit, $R_{\rm min}$ (where this is not marked $R_{\rm min} = 0$). The blue and green lines show the rotation curve contribution from stars and gas, respectively. The top three panels show fits using our coreNFW profile that accounts for cusp-core transformations due to stellar feedback (see Section 4.2). These give an excellent fit to the rotation curve shape in all three cases. The bottom three panels show fits using an NFW profile, where we set $R_{\rm min}$ to ensure that the outer rotation curve is well fitted. This gives a much poorer fit to the rotation curve shape, reaffirming the longstanding 'cusp-core' problem.

of isolated dIrrs that we consider here. There is, however, one significant outlier, DDO 154. We discuss this interesting galaxy further in Section 6.

### 5.3 The stellar mass function in groups and in the field

In this section, we compare four stellar mass functions taken from the literature, as reported in Fig. 1. The blue data points show the stellar mass function from SDSS (Behroozi et al. 2013), the red data points from GAMA (Baldry et al. 2012), the black data points from RT05 and the magenta data points from zCOSMOS (Giodini et al. 2012). (See Section 3 for a description of these surveys.) The green tracks show a non-parametric fit to the SDSS stellar mass function, where the upper and lower tracks encompass the 68 per cent confidence intervals of the data. Below $M_\star = 10^8$ M$_\odot$, we fit a single power law to the SDSS data and use this to extrapolate to lower stellar mass. As in Baldry et al. (2008), we find a best-fitting logarithmic slope of $\alpha = 1.6$, where $dN/dM|_{M_*<10^8\,{\rm M}_\odot} \propto M^{-\alpha}$.

#### *5.3.1 Evidence for a shallower group stellar mass function below $M_\star \sim 10^9\,M_\odot$*

First, notice that below $M_\star \sim 10^9$ M$_\odot$ the SDSS and RT05 stellar mass functions diverge, with the RT05 mass function becoming substantially shallower. This difference has been noted previously in the literature (e.g. Baldry et al. 2008) but to date has remained unexplained. Here, we suggest that it owes to an *environmental* dependence. The RT05 stellar mass function was built using a compilation of SDSS data at the bright end, and the luminosity function of the Trentham & Tully (2002) *local groups catalogue* at the faint end (see Section 3.2). Thus, by construction, below $M_\star \sim 10^9$ M$_\odot$ RT05 measured the stellar mass function of nearby galaxy groups. Indeed, we find further evidence for this from the zCOSMOS survey. Giodini et al. (2012) split the zCOSMOS stellar mass function into a 'field galaxy' sample (Fig. 1; magenta circles) and an X-ray selected group sample (magenta diamonds) over the redshift range $z = 0.2$–$0.4$. As can be seen in Fig. 1, the zCOSMOS stellar mass functions are only complete down to $M_\star \sim 4 \times 10^8$ M$_\odot$ (see Section 3) but nonetheless, at this mass scale, there is a statistically significant bifurcation between the zCOSMOS field and group samples that matches that seen in SDSS and RT05.

There are two key challenges involved in comparing zCOSMOS with RT05 and SDSS. First, the redshift range of the surveys is different (see Section 3). However, this is not a significant effect since the stellar mass function is known to be almost constant out to $z = 0.5$ (Behroozi et al. 2013). (Indeed, we find no difference between the zCOSMOS field stellar mass function (magenta circles) and that of SDSS (blue data points) down to $M_\star \sim 4 \times 10^8$ M$_\odot$.)

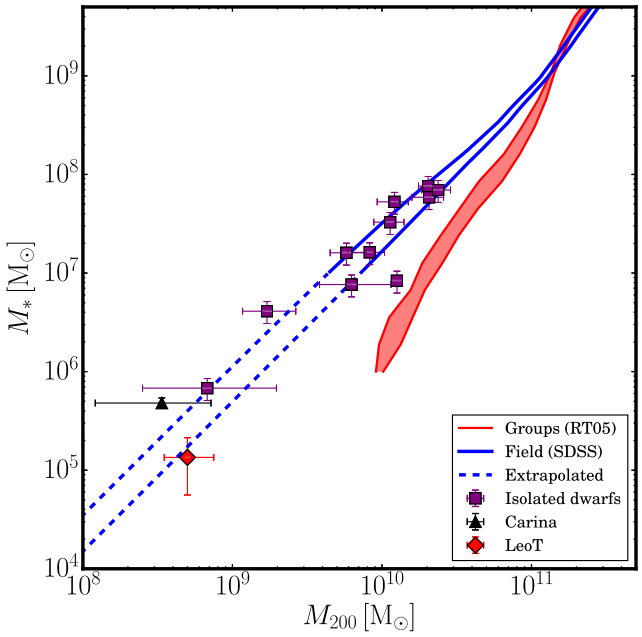


**Figure 3.** The stellar mass–halo mass relation of 11 isolated dIrr galaxies, derived from their H I rotation curves ($M_\star$–$M_{200}|_{\rm rot}$), and two galaxies that do not have H I rotation curves: the isolated dwarf irregular Leo T (diamond) and the Milky Way dwarf spheroidal galaxy Carina (black triangle). (The masses of these two galaxies are derived as described in Section 3.) All data are reported in Table 2. Overplotted are $M_\star$–$M_{200}|_{\rm abund}$ calculated from abundance matching in ΛCDM using the SDSS field stellar mass function (solid blue lines) and the RT05 stellar mass function of nearby groups (red shaded region). The lines are dashed where they rely on a power-law extrapolation of the SDSS stellar mass function below $M_\star \sim 10^7$ M$_\odot$. Notice that $M_\star$–$M_{200}|_{\rm abund}$ (blue lines) gives a remarkable match to $M_\star$–$M_{200}|_{\rm rot}$ (purple data points) down to $M_{200} \sim 5 \times 10^9$ M$_\odot$, and $M_{200} \sim 5 \times 10^8$ M$_\odot$ if we use the power-law extrapolation of the SDSS stellar mass function (dashed lines). However, $M_\star$–$M_{200}|_{\rm abund}$ derived from the stellar mass function of nearby galaxy groups (red shaded region) gives a poor match.

Secondly, the definition of a 'group' differs. The Giodini et al. (2012) groups are selected based on co-added *XMM* and *Chandra* X-ray images, using a wavelet method to detect extended emission (Finoguenov et al. 2007). In this way, they find groups over the mass range $0.14 < M_{500}/(10^{13}{\rm M}_\odot) < 26$. By contrast, Trentham & Tully (2002) study five nearby optically selected groups, including the Local Group. Only one of these has reported X-ray emission (Romanowsky et al. 2009), but they do span a similar mass range to the Giodini et al. (2012) sample (Zhang et al. 2007; Makarov & Karachentsev 2011; Peñarrubia et al. 2016). For these reasons, a direct comparison between the Trentham & Tully (2002) and Giodini et al. (2012) groups is reasonable. Indeed, their stellar mass functions agree remarkably well down to the stellar mass limit of the zCOSMOS survey (compare the magenta diamonds and black data points in Fig. 1).

Finally, consider the GAMA stellar mass function in Fig. 1 (red data points). This agrees well with both the zCOSMOS field sample (magenta circles) and SDSS (blue data points) down to $M_\star \sim 2 \times 10^8$ M$_\odot$. The one data point below this is slightly, though not statistically significantly, shallower than SDSS. It is beyond the scope of this present work to explore this discrepancy in any detail, though it has been noted previously (e.g. Baldry et al. 2012). As emphasized in Section 3, the GAMA survey covers about one tenth of the volume of SDSS and is complete only at a higher stellar mass. For these reasons, we will use the SDSS stellar mass function for the remainder of this paper. We discuss the GAMA stellar mass function further in Section 6.

### 5.3.2 *The origin of the $M_\star \sim 10^9$ M$_\odot$ mass scale*

The shallower group stellar mass function that we find here is perhaps not surprising. It has long been known that satellites are quenched on infall to groups due to a combination of ram-pressure stripping and tides (e.g. Peng et al. 2012; Gatto et al. 2013; Carollo et al. 2013). Ram pressure shuts down star formation, leading to a lower stellar mass for a given pre-infall halo mass, while tides physically destroy haloes depleting the dark matter subhalo mass function. In the Milky Way, this is evidenced by the 'distance–morphology' relation: most satellites within ∼200 kpc of the Galactic Centre have truncated star formation and are devoid of gas, while those at larger radii have H I and are currently forming stars (e.g. Haynes, Giovanelli & Chincarini 1984; Mateo 1998; Mayer et al. 2001b; Grebel, Gallagher & Harbeck 2003; Tolstoy, Hill & Tosi 2009; McConnachie 2012; Gatto et al. 2013).

It is interesting to ask, however, whether ram pressure or tides can explain why the stellar mass function is affected only below $M_\star \sim 10^9$ M$_\odot$. In R16a, we calculated the effect of tides on satellites orbiting within a Milky Way mass host (their section 4.3). The effect is maximized if satellites have their dark matter cusps transformed into cores. But even in this extremum limit, satellites are only fully destroyed if they have a pericentre of $r_{\rm p} \lesssim 30$ kpc and a mass $M_{200} \lesssim 10^{10}$ M$_\odot$. Using our $M_\star$–$M_{200}|_{\rm rot}$ relation in Fig. 3, this corresponds to a stellar mass of $M_\star \sim 2 - 3 \times 10^7$ M$_\odot$, suggesting that tides are not likely to be the primary cause of the shallower group stellar mass function that we find here.

The second potential culprit is ram pressure. This occurs when (Gatto et al. 2013):

$$\rho_{\rm h}(r_{\rm p}) v_{\rm p}^2 \gtrsim \frac{1}{5}\rho_{\rm d}\frac{v_{\rm max}^2}{2} \qquad (12)$$

where $\rho_{\rm h}$ is the coronal gas density of the host at pericentre; $v_{\rm p}$ is the velocity of the satellite at pericentre; $\rho_{\rm d}$ is the density of gas in the dwarf ISM; $v_{\rm max}$ is the peak rotational velocity of the dwarf[4] and the factor 1/5 accounts for non-linear effects (Gatto et al. 2013).

For a satellite falling into the Milky Way, $\rho_{\rm h} \sim 3 \times 10^{-4}$ atoms cm$^{-3}$; $v_{\rm p} \sim 450$ km s$^{-1}$; and $\rho_{\rm d} \sim 0.1$ atoms cm$^{-3}$ (Gatto et al. 2013). Thus, we can rearrange equation (12) to provide a limiting $v_{\rm max}$ below which ram pressure becomes important:

$$v_{\rm max,ram} = \sqrt{\frac{10\rho_{\rm h}}{\rho_{\rm d}}}\, v_{\rm p} \sim 78\,{\rm km\,s^{-1}}. \qquad (13)$$

This is similar to the $v_{\rm max}$ of the LMC (van der Marel et al. 2002) that has a stellar mass of $M_\star \sim 1.5 \times 10^9$ M$_\odot$ (McConnachie 2012). This suggests that the shallower group stellar mass function that we find here owes to satellite quenching, driven primarily by ram pressure. Indeed, Geha et al. (2012) found, using SDSS data, that *all* field galaxies above $M_\star = 10^9$ M$_\odot$ are star-forming today, independent of environment. By contrast, galaxies with $M_\star < 10^9$ M$_\odot$ can be

[4] We have assumed here that $v_{\rm max}^2 \simeq 2\sigma_*^2$, where $\sigma_\star$ is the stellar velocity dispersion of the dwarf. This amounts to an assumption of a flat, isothermal, rotation curve for the dwarf (e.g. Binney & Tremaine 2008).

quenched, with the quenched fraction increasing with proximity to a larger host galaxy.

### 5.4 Abundance matching in groups and in the field

In this section, we measure $M_\star$–$M_{200}|_{\rm abund}$ using the stellar mass functions in Fig. 1 matched to the ΛCDM Bolshoi simulation (Klypin et al. 2011). Our abundance matching is 'non-parametric' in the sense that we numerically integrate the curves in Fig. 1 to obtain the cumulative stellar mass function; we then match these numerically to the cumulative halo mass function from the Bolshoi simulation. For this latter, we use a Schechter function fit to the halo mass function, defining the 'halo mass' as the virial mass $M_{200}$ before infall.

The results are shown in Fig. 3 for the SDSS field stellar mass function (blue lines) and the RT05 group stellar mass function (red shaded region). The lines are dashed where they rely on a power-law extrapolation of the SDSS stellar mass function below $M_\star \sim 10^7$ M$_\odot$. (We compare and contrast our abundance matching results with previous determinations in the literature in Appendix C.)

Notice that $M_\star$–$M_{200}|_{\rm abund}$ (blue lines) gives a remarkable match to $M_\star$–$M_{200}|_{\rm rot}$ (purple data points) down to $M_{200} \sim 5 \times 10^9$ M$_\odot$, and $M_{200} \sim 5 \times 10^8$ M$_\odot$ if we use the power-law extrapolation of SDSS. However, $M_\star$–$M_{200}|_{\rm abund}$ derived from the stellar mass function of nearby galaxy groups (RT05; red shaded region) gives a poor match. In particular, it leads to the familiar result that all dwarf galaxies must inhabit implausibly massive $\sim 10^{10}$ M$_\odot$ haloes (e.g. Read et al. 2006) that has become known as the 'too big to fail' (TBTF) problem (e.g. Boylan-Kolchin et al. 2011).

There are a number of problems with using the RT05 stellar mass function for 'classical' abundance matching as we have done here. First, we have assumed a monotonic relation between $M_\star$ and $M_{200}$. We have shown that this is true for our sample of isolated dIrrs (Section 5.2), but we expect it to fail for satellites whose $M_\star$ will depend on $M_{200}$, their time of infall and their orbit, inducing scatter in $M_\star$ for a given pre-infall $M_{200}$ (e.g. Ural et al. 2015; Tomozeiu, Mayer & Quinn 2016; Garrison-Kimmel et al. 2017, and see Section 5.3.2). Secondly, there is what we might call a 'volume problem'. If we wish to match a pure-dark matter simulation to the Milky Way, what volume should we use to normalize the Milky Way satellite mass function? Brook et al. (2014) and Garrison-Kimmel et al. (2014, hereafter G-K14) solve this by explicitly matching satellites to constrained simulations of the Local Group. Here, we solve it by using the RT05 stellar mass function. This solves the 'volume problem' by renormalizing the group stellar mass functions derived from Trentham & Tully (2002) to match SDSS at the bright end (see Section 3). Since this normalizes the volume to SDSS field galaxies, we must then abundance match RT05 with the full Bolshoi simulation, as we have done here. Indeed, in Appendix C we verify that our RT05 $M_\star$–$M_{200}|_{\rm abund}$ relation, derived in this way, agrees very well with those derived independently by Brook et al. (2014) and G-K14. Finally, there is the problem of satellite quenching. As discussed in Section 5.3.2, satellites can have their star formation shut down by ram-pressure stripping, or be tidally disrupted on infall. Tidal stripping is already dealt with, in part, by using the pre-infall $M_{200}$ (e.g. Diemand, Kuhlen & Madau 2007). However, we expect tidal disruption to be enhanced by cusp-core transformations and the presence of the stellar disc, neither of which are captured by pure dark matter simulations (e.g. Read et al. 2006; D'Onghia et al. 2010; Peñarrubia et al. 2010; Zolotov et al. 2012; Wetzel et al. 2016, and see the discussion in R16a).

For all of the above reasons, we expect 'classical' abundance matching with the RT05 stellar mass function to fail. Nonetheless, it is instructive because the key assumptions that go into it are common in the literature (e.g. G-K14; Brook et al. 2014). Indeed, it is likely that these assumptions are responsible for the now longstanding 'missing satellites' and TBTF problems that manifest for satellite galaxies below $M_{\rm TBTF} \sim 10^{10}$ M$_\odot$ (Read et al. 2006; Boylan-Kolchin, Bullock & Kaplinghat 2011; Tollerud, Boylan-Kolchin & Bullock 2014, and see Section 1). The fact that $M_\star$–$M_{200}|_{\rm rot}$ matches $M_\star$–$M_{200}|_{\rm abund}$ for our sample of isolated dIrrs demonstrates that every isolated field halo is occupied with a dIrr down to $M_{200} \sim 5 \times 10^9$ M$_\odot$ and to $M_{200} \sim 5 \times 10^8$ M$_\odot$ if we use the power-law extrapolation of SDSS. Furthermore, these dwarfs inhabit dark matter haloes that are perfectly consistent with their observed gaseous rotation curves. Thus, our sample of isolated dIrrs – that extend to $M_{200} < M_{\rm TBTF}$ – has no missing satellites or TBTF problem, suggesting that both depend on *environment*. We discuss this further in Section 6.

### 5.5 Constraints on warm dark matter

We have shown so far that the field dIrr $M_\star$–$M_{200}|_{\rm abund}$ is consistent with $M_\star$–$M_{200}|_{\rm rot}$ in ΛCDM. In this section, we consider how well these match in a ΛWDM cosmology. We use the formulae in Schneider et al. (2012) to transform the Bolshoi halo mass function, derived for ΛCDM, to one in ΛWDM[5]:

$$\left.\frac{{\rm d}N}{{\rm d}M}\right|_{\rm WDM} = \left.\frac{{\rm d}N}{{\rm d}M}\right|_{\rm CDM} \left(1 + \frac{M_{\rm hm}}{M}\right)^{-\beta} \quad (14)$$

where $M_{\rm hm} = 4/3\pi\rho_{\rm crit}(\lambda_{\rm hm}/2)^3$ is the 'half mode mass', $\beta = 1.16$, $\lambda_{\rm hm}$ is the 'half mode' scalelength, given by:

$$\lambda_{\rm hm} = 0.683 \left(\frac{m_{\rm WDM}}{\rm keV}\right)^{-1.11} \left(\frac{\Omega_{\rm M}}{0.25}\right)^{0.11} \left(\frac{h}{0.7}\right)^{1.22} {\rm Mpc}\, h^{-1}, \quad (15)$$

where $m_{\rm WDM}$ is the warm dark matter particle mass in keV, $\Omega_{\rm M}$ is the matter density of the Universe at redshift $z = 0$, and $h$ is the Hubble parameter (we assume the same cosmological parameters as in the Bolshoi simulation; see Table 1.).

In Fig. 4, we show tracks of $M_\star$–$M_{200}|_{\rm abund}$ in ΛWDM for varying thermal relic mass over the range $1 < m_{\rm WDM} < 5$ keV, as marked (green lines). Where these lines rely on the extrapolated SDSS stellar mass function, they are dashed. We deliberately pick the most conservative limits by using the lower bound of the SDSS stellar mass function to calculate $M_\star$–$M_{200}|_{\rm abund}$.

As can be seen from Fig. 4, without using the power-law extrapolation of the SDSS stellar mass function below $M_\star \sim 10^7$ M$_\odot$, we can rule out $m_{\rm WDM} < 1.25$ keV at 68 per cent confidence. Using the power-law extrapolation, this limit improves to $m_{\rm WDM} < 2$ keV at 68 per cent confidence. If we further add the Leo T data point, then this tightens to $m_{\rm WDM} < 3$ keV. However, for this limit to become

5 There is a known problem in the literature with the formation of spurious haloes at the resolution limit in WDM simulations (e.g. Wang & White 2007; Angulo, Hahn & Abel 2013; Hahn, Abel & Kaehler 2013; Lovell et al. 2014; Hobbs et al. 2016). Equation (14) is derived from fits to *N*-body simulations where such spurious haloes have been pruned from the analysis. We refer to it as describing an 'effective warm dark matter' cosmology because it really describes a suppression in the halo mass function at low mass, parametrized by an effective thermal relic mass, $m_{\rm WDM}$. More realistic WDM models will show model-specific features in the small-scale matter power spectrum (see e.g. Boyarsky et al. 2009 for sterile neutrino models). It is beyond the scope of this present work to test such models in detail.

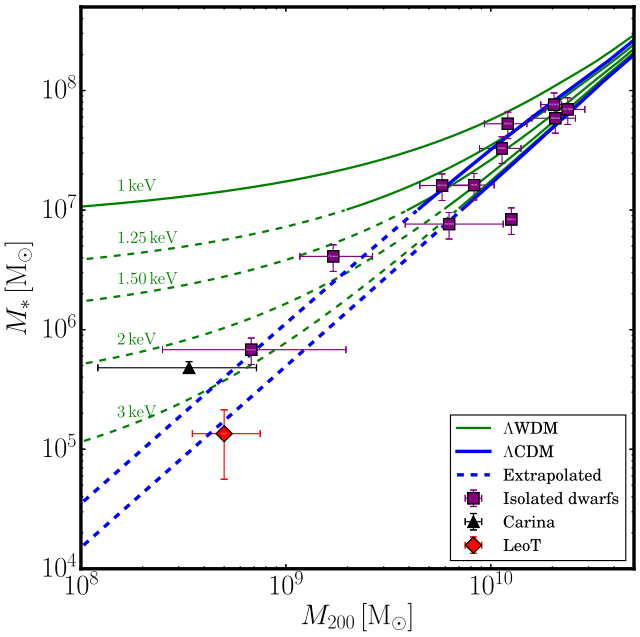


**Figure 4.** $M_\star$–$M_{200}|_{\rm rot}$ (purple data points) as compared to $M_\star$–$M_{200}|_{\rm abund}$ in ΛCDM (blue lines) and ΛWDM (green lines), using the SDSS field stellar mass function. The thermal relic mass $m_{\rm WDM}$ is marked on the curves in keV. The lines and symbols are as in Fig. 3.

robust we would need to find many more Leo T-like galaxies in the Local Volume, ideally with measured rotation curves. We discuss this further in Section 6.

Our limit on $m_{\rm WDM}$ approaches the latest limits from the Lyman $\alpha$ forest (e.g. Baur et al. 2016). It is competitive with a more model-dependent limit from Local Group satellite galaxies (e.g. Anderhalden et al. 2013) and a recent constraint from the high-redshift UV luminosity function (Menci et al. 2016). We discuss how our constraint will improve with a deeper stellar mass function and/or a complete census of low-mass isolated dwarfs in Section 6.

## 6 DISCUSSION

### 6.1 A shallower group stellar mass function below $M_\star \sim 10^9$ M$_\odot$

In Section 5.3, we argued that the stellar mass function is shallower in groups below $M_\star \sim 10^9$ M$_\odot$. It has been noted already in the literature that there are significant differences in both the luminosity and stellar mass functions of galaxy clusters and field galaxies (e.g. Trentham 1998; Xia et al. 2006; Bolzonella et al. 2010; Peng et al. 2010, 2012; Eckert et al. 2016). However, a similar such environmental dependence on group scales has proven more elusive. Using SDSS data, Yang, Mo & van den Bosch (2009) found no difference between the stellar mass function in groups and the field. However, they were only complete down to $M_\star \sim 10^9$ M$_\odot$ and so would not have been able to detect the difference that we find here. In principle, it should be possible to split the SDSS luminosity function in Blanton et al. (2005) into a group and field sample to test our findings, but this is beyond the scope of this present work. As we noted in Section 5.3, it is compelling that Geha et al. (2012) report a field galaxy quenching mass scale of $M_\star = 10^9$ M$_\odot$ that depends on proximity to a larger host galaxy. This is precisely the stellar mass scale at which we calculated that ram-pressure stripping will become important (Section 5.3.2), and it is precisely the mass scale at which we find a suppression in the group stellar mass function. We will explore these ideas further in future work.

### 6.2 The missing satellite problem and TBTF in groups and the field

We have shown that abundance matching in ΛCDM is consistent with isolated dwarf galaxy rotation curves down to $M_{200} \sim 5 \times 10^9$ M$_\odot$, and $M_{200} \sim 5 \times 10^8$ M$_\odot$ if we assume a power-law extrapolation of the SDSS stellar mass function. A direct corollary of this is that every single halo in the field is occupied with a galaxy down to these limits and, furthermore, that their gas dynamics are consistent with the halo that they live in. This means that there is *no 'missing satellites' or TBTF problem in the field down to these limits.*

The above is interesting because both the missing satellites and TBTF problems occur in the Milky Way and Andromeda satellite population below a mass scale of $M_{\rm TBTF} \sim 10^{10}$ M$_\odot$ (Read et al. 2006; Boylan-Kolchin et al. 2011; Tollerud et al. 2014). If there is no similar problem at this mass scale for isolated 'field' galaxies, then both problems must owe to some *environmental effect*. Indeed, a likely culprit is quenching due to ram pressure on infall to groups, as we have discussed already in Section 5.3.2. It is beyond the scope of this paper to determine whether or not such environmental processes can fully solve the missing satellites and TBTF problems inside groups. However, it is hard to understand how some change to the underlying cosmological model could act inside groups but not in the field. For this reason, we assert that both of these small-scale puzzles must owe to 'galaxy formation physics', rather than exotic cosmology.

A final implication of the above result is that we expect significant scatter in $M_\star$ for a given pre-infall $M_{200}$ inside groups. This means that, inside groups, classical 'monotonic' abundance matching will fail (see also Ural et al. 2015; Tomozeiu et al. 2016). However, more sophisticated mappings between dark and luminous subhaloes that take account of the radial or orbit distribution of satellites could still work (e.g. Lux, Read & Lake 2010; Macciò et al. 2010; Anderhalden et al. 2013). Similarly, it may be possible to build a working abundance matching model that simply introduces significant scatter in the $M_\star - M_{200}$ relation below some stellar mass scale (e.g. Jethwa, Belokurov & Erkal 2016; Garrison-Kimmel et al. 2017, and see Appendix C).

### 6.3 Comparison with other works

Our result that there is no missing satellites or TBTF problem for field dIrrs is apparently at odds with Klypin et al. (2015) and Papastergis et al. (2015) who report a severe abundance/TBTF problem in the Local Volume. To arrive at this conclusion, both studies compare the distribution function of H I velocity line widths of a sample of Local Volume galaxies with predictions from the Bolshoi simulation. However, this relies on being able to convert H I velocity line widths to the peak rotation velocity of dark matter haloes, $v_{\rm max}$. Brook & Shankar (2016) have argued that this conversion is complex, particularly for dwarfs with $v_{\rm max} < 50$ km s$^{-1}$. With reasonable assumptions, they find that they can reconcile ΛCDM with the data in Klypin et al. (2015) (and see also Papastergis & Shankar 2016). Recently, however, Trujillo-Gomez et al. (2016) have revived the debate. They take similar care with the conversion from H I line widths to $v_{\rm max}$, accounting for 'cusp-core' transformations due to stellar feedback. Yet, they find that the Local Volume

abundance problem persists. It is beyond the scope of this work to explore this further, but we note that if the stellar mass function is shallower inside groups, then it is likely to be suppressed also on the $\sim$10 Mpc$^3$ scale of the Local Volume. If this is the case, then Local Volume galaxies should lie on the $M_\star$–$M_{200}|_{\rm rot}$ relation that we find here, but have a stellar mass function that is shallower than SDSS.

Our results are also in tension with the higher redshift study of Miller et al. (2014). They derive an $M_\star$–$M_{200}|_{\rm rot}$ relation for galaxies over the redshift range $0.2 < z < 1$, finding a significant offset from $M_\star$–$M_{200}|_{\rm abund}$. However, due to the higher redshift of their galaxy sample, they have only a single measure of the rotational velocity at 2.2 disc scalelengths. This is then extrapolated to the velocity at the virial radius $V_{200}$ via a weak lensing calibration at a stellar mass of $\log_{10}[M_\star/{\rm M}_\odot] = 9.0$. As highlighted by Miller et al. (2014), this could introduce a potentially large systematic error. Furthermore, it is challenging with just a single measurement of the rotation velocity to identify 'rogues' (see Figs A1–A3). We will explore the Miller et al. (2014) data further in future work.

More similar to our analysis here is the recent study of P16. They use the baryon-influenced mass models from Di Cintio et al. (2014) to fit rotation curves and measure $M_{200}$ and $c$ for a large sample of dwarfs in the Little THINGS and THINGS surveys. Comparing their results with abundance matching predictions, similarly to our analysis here, they arrive at the opposite conclusion that $\Lambda$CDM is inconsistent with the data. Our analyses are sufficiently different that a detailed comparison is somewhat challenging, but we note here three key differences that likely lead to this apparent discrepancy: (i) P16 use the Little THINGS and THINGS rotation curves, whereas we derive the rotation curves using $^{\rm 3D}$BAROLO (Iorio et al. 2016); (ii) P16 use the Di Cintio et al. (2014) model that does not show cusp-core transformations below $M_{200} \sim 10^{10}$ M$_\odot$, whereas we use the coreNFW profile from R16a that does; and (iii) P16 primarily compare their results with $M_\star$–$M_{200}|_{\rm abund}$ from G-K14, whereas we favour matching the SDSS stellar mass function to the Bolshoi simulation. The most significant of these is (iii). The G-K14 $M_\star$–$M_{200}|_{\rm abund}$ relation relies on *Local Group galaxies*. This is problematic since – as we argued in Section 5.4 – classical abundance matching is expected to fail inside groups. Indeed, using the RT05 group stellar mass function, we derive an (erroneous) $M_\star$–$M_{200}|_{\rm abund}$ relation that is remarkably similar to that derived in G-K14, and a similar relation derived in Brook et al. 2014 (see Appendix C).

A similar critique explains the apparent discrepancy between our findings here and the earlier work of Ferrero et al. (2012). They find, in agreement with us, that galaxies with stellar mass $M_\star \lesssim 3 \times 10^7$ M$_\odot$ inhabit haloes with mass $M_{200} \lesssim 10^{10}$ M$_\odot$. However, they argue that this is at odds with abundance matching in $\Lambda$CDM. Similarly to P16, this is because they use a steep $M_\star$–$M_{200}|_{\rm abund}$ that is similar to our erroneous RT05 'group' relation. Using the shallower field galaxy SDSS $M_\star$–$M_{200}|_{\rm abund}$, the Ferrero et al. (2012) results are in good agreement with ours.

Finally, Katz et al. (2017) have recently compared the Di Cintio et al. (2014) model to data for 147 rotation curves from the SPARC sample. Comparing their derived $M_\star$–$M_{200}|_{\rm rot}$ relation with $M_\star$–$M_{200}|_{\rm abund}$, they conclude similarly to us here that $\Lambda$CDM works very well. In this case, there is no discrepancy. Katz et al. (2017) focus on galaxies that are substantially more massive than those we study here, with $M_{200} > 10^{10}$ M$_\odot$. In this sense, the Katz et al. (2017) study is wholly complementary to ours that focuses on the regime $M_{200} < 10^{10}$ M$_\odot$.

### 6.4 The interesting outlier DDO 154

As discussed in Section 5.2, our $M_\star$–$M_{200}|_{\rm rot}$ relation in Fig. 3 has one significant outlier, DDO 154. This galaxy also has an unusually high H I gas mass fraction, with $M_{\rm HI}/M_* = 37$. At its currently observed star formation rate of $\dot{M}_* = 3.82 \times 10^{-3}$ (Zhang et al. 2012), DDO 154 would move on to our $M_\star$–$M_{200}|_{\rm rot}$ relation in $\sim$5.7 Gyr. This is an interesting time-scale. In $\Lambda$CDM, most major galaxy mergers are complete by redshift $z = 1$ some $\sim$8 Gyr ago (e.g. Stewart et al. 2009). Thus, if post-merger isolated dwarfs look like DDO 154, then most would have had time to deplete their excess H I gas and move on to the $M_\star$–$M_{200}|_{\rm rot}$ relation by today. A possible explanation for DDO 154, then, is that it has just undergone a relatively rare late merger. We will explore this idea further in future work.

### 6.5 How close is too close?

It is interesting to ask *how close* to the Milky Way satellites can orbit before they become quenched. The Carina dwarf spheroidal is particularly interesting in this regard. Its orbit remains highly uncertain due to its large proper motion errors, but Lux et al. (2010) find that it seems to be substantially more circular than the mean of subhaloes in a $\Lambda$CDM pure dark matter simulation. With an apo-to-pericentre ratio of $r_{\rm p}/r_{\rm a} = 0.3 - 0.7$, it is also potentially more circular than all of the other Milky Way dwarfs, except one: Fornax. Fornax is on a cosmologically unusual near circular orbit, with $r_{\rm p}/r_{\rm a} \sim 0.6$–$0.8$ (Lux et al. 2010). Along with Carina, it is the only other Milky Way dwarf spheroidal that has continued to form stars for nearly a Hubble time (del Pino et al. 2013). Such circularity may be the key to these dwarfs' ability to continue to form stars, lending further support to the idea that quenching is driven primarily by ram pressure. From equation (12), we can see that ram pressure is proportional to the satellite velocity at pericentre squared: $v_{\rm p}^2$. Circular orbits minimize $v_{\rm p}$ and will therefore also minimize the effect of ram-pressure stripping. The fact that Carina appears to lie on the $M_\star$–$M_{200}|_{\rm rot}$ relation of isolated dwarfs suggests that it has come just about as close to the Milky Way as possible while maintaining its ability to form stars. This may help to explain its puzzlingly unique star formation history (de Boer et al. 2014).

### 6.6 Implications for cusp-core transformations at low stellar mass

In R16a, we found that dark matter cusp-core transformations for isolated dwarfs continue down to at least $M_\star \sim 5 \times 10^5$ M$_\odot$ ($M_{200} \sim 5 \times 10^8$ M$_\odot$), under the assumption that reionization does not shut down star formation at this mass scale (see Sections 1 and 6.7 for more discussion on this point). However, several works in the literature have claimed that there is insufficient energy in such low stellar mass systems for cusp-core transformations to proceed (e.g. Peñarrubia et al. 2012; Garrison-Kimmel et al. 2013; Di Cintio et al. 2014; Tollet et al. 2016). We are now in a position to revisit this problem. As discussed in R16a, the main difference between all of the studies in the literature to date has been in the stellar mass to halo mass relation (either assumed or self-consistently calculated using hydrodynamic simulations). The more stars a given halo forms, the more supernovae it has to unbind its dark cusp.

Following Peñarrubia et al. (2012) and R16a, we may estimate the supernova energy that is available to transform cusps to cores as:

$$\Delta E = \frac{E_{\rm SN} M_*}{\langle m_* \rangle} \xi(m_* > 8\,{\rm M}_\odot) \epsilon_{\rm DM} \qquad (16)$$

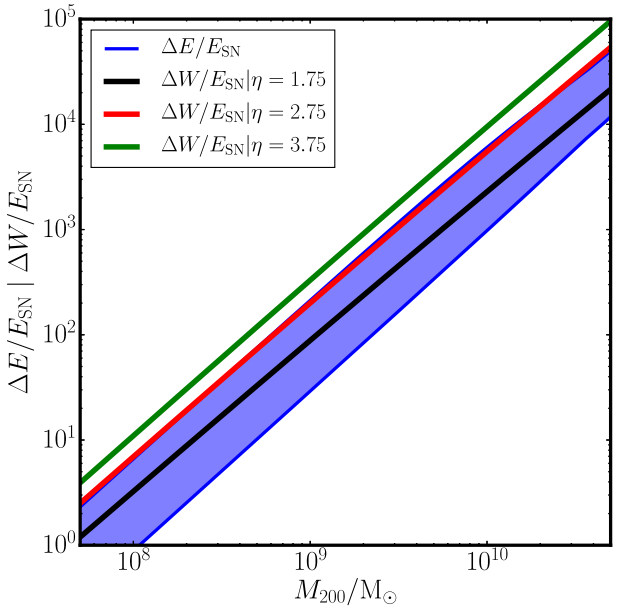


**Figure 5.** The supernova energy available for driving dark matter cusp-core transformations (blue band) compared to the energy required to unbind the dark matter cusp (black, red and green lines), as a function of dark matter halo mass $M_{200}$. The black line shows results for our default dark matter core size of $\eta = 1.75$ (equation 11). The red and green lines show results for larger dark matter cores with $\eta = 2.75$ and $\eta = 3.75$, respectively. The energies are plotted in units of a single supernova explosion ($E_{\rm SN}$). For our default dark matter core size ($\eta = 1.75$) there is sufficient energy from SNe explosions at all mass scales to excite cusp-core transformations 'all the way down'.

where $E_{\rm SN} = 10^{51}$ erg is the energy of a single supernova; $\langle m_\star \rangle = 0.83\,{\rm M}_\odot$ is the mean stellar mass; $\xi = 0.00978$ is the fraction of mass in stars that go supernova[6] and $\epsilon_{\rm DM} \simeq 0.25 - 0.8$ per cent is the efficiency of coupling of the SNe energy to the dark matter. (We estimate $\epsilon_{\rm DM}$ using the simulations in R16a. Following R16a, this is defined as the ratio of the energy required to unbind the dark matter cusp to the integrated supernovae energy.)

The available supernova energy can then be compared with the energy required to unbind the dark matter cusp:

$$\Delta W = -\frac{1}{2}\int_0^\infty \frac{G(M_{\rm NFW}^2 - M_{\rm cNFW}^2)}{r^2}{\rm d}r \qquad (17)$$

where $M_{\rm NFW}$ and $M_{\rm cNFW}$ are the enclosed cumulative mass for an NFW and coreNFW dark matter density profile, respectively (equations 7 and 6).

The available energy (equation 16) depends on the galaxy stellar mass $M_\star$, while the required energy to unbind the cusp (equation 17) depends on the halo mass $M_{200}$. Hence, the $M_\star - M_{200}$ relation is critical. Using the $M_\star$–$M_{200}|_{\rm abund}$ relation from Fig. 3, we plot $\Delta E(M_{200})$ and $\Delta W(M_{200})$ in Fig. 5. We assume that the stellar half-mass radius is given by $R_{1/2} \sim r_{1/2} \sim 0.015 r_{200}$ (Kravtsov 2013; Agertz & Kravtsov 2016; Shibuya, Ouchi & Harikane 2015), that the total star formation time $t_{\rm SF} = 14$ Gyr such that core formation is complete, that haloes obey the concentration mass relation from Macciò et al. (2007) and that the birth stellar mass (i.e. before mass loss due to stellar evolution) is approximately two times the current stellar mass (see R16a).

[6] As in R16a, we assume a Chabrier (2003) IMF averaged over the range $0.1 < m_\star/{\rm M}_\odot < 100$.

The results are shown in Fig. 5, where the blue band marks the available supernova energy as a function of halo mass $M_{200}$, while the black, red and green lines mark the energy required to unbind the cusp. The black line shows results for our default dark matter core size of $\eta = 1.75$ (equation 11). The red and green lines show results for larger dark matter cores with $\eta = 2.75$ and $\eta = 3.75$, respectively. As can be seen, there is sufficient energy to unbind a dark matter cusp 'all the way down' for $\eta < 2.75$, but insufficient energy to build larger cores than this.

These results support our assertion in R16a that dark matter cores can form 'all the way down'. However, this is only energetically possible if isolated low-mass haloes are largely unaffected by reionization. We discuss this, next.

### 6.7 But what about reionization?

Our results suggest that all field dark matter haloes are occupied with galaxies down to $M_{200} \sim 5 \times 10^8$ M$_\odot$ (if we assume a power-law extrapolation of the SDSS stellar mass function). Indeed, Leo T – which appears to sit at this mass scale – has formed stars continuously at a rate of just $\sim 10^{-5}$ M$_\odot$ yr$^{-1}$ for a Hubble time (Weisz et al. 2012b). If Leo T does inhabit such a low-mass halo, then a corollary of this is that reionization does not appear to suppress galaxy formation above $M_{\rm reion} \sim 5 \times 10^8$ M$_\odot$. This is in excellent agreement with recent models by Gnedin & Kaurov (2014), but at tension with other simulations that favour a substantially higher $M_{\rm reion} \gtrsim 3 \times 10^9$ M$_\odot$ (e.g. Simpson et al. 2013; Wheeler et al. 2015; Fitts et al. 2016; Ocvirk et al. 2016; Sawala et al. 2016a).

The above tension is not necessarily a cause for concern. There is a least a factor of 2–4 uncertainty in the flux of ionizing photons at high redshift, with galaxies being the dominant ionizing source at $z \gtrsim 3$ and quasars dominating at lower redshifts (e.g. Haardt & Madau 2012). Large volume simulations are required to capture these photon sources correctly. These require very high spatial resolution and accurate ray propagation to model self-shielding effects and to correctly predict the photon escape fraction, $f_{\rm esc}$ (e.g. Gnedin 2016). In particular, Kimm & Cen (2014) found, using high-resolution simulations of galaxies forming in haloes with virial masses $\sim 10^8$–$10^{10}$ M$_\odot$ at $z \gtrsim 7$, that $f_{\rm esc}$ fluctuates by orders of magnitude over a dynamical time due to stellar feedback (and see also Trebitsch, Blaizot & Rosdahl 2015). Numerical resolution is also important. Bland-Hawthorn, Sutherland & Webster (2015) find that reionization blows out far more gas in low-resolution simulations as compared to higher resolution simulations that better-capture dense gas. Finally, it is important to include all of the important physics. Ricotti (2009) highlight the importance of adiabatic cooling due to the expansion of the Universe, while Vandenbroucke, Verbeke & De Rijcke (2016) suggest that additional feedback due to Population III stars could reduce early star formation and feedback, leading to less hot diffuse gas and less reionization-driven gas blow out. It is beyond the scope of this present work to explore these ideas in more detail. We simply note here that at present there is no cause for concern if Leo T inhabits a dark matter halo of mass $M_{200} \sim 5 \times 10^8$ M$_\odot$.

### 6.8 Implications for near-field cosmology

Our results allow us to make several concrete predictions for upcoming near-field cosmology surveys:

(i) First, assuming that ΛCDM is correct, we predict that the stellar mass function of field galaxies should continue as an

unbroken power law with slope $\alpha \sim 1.6$, at least over the mass range $10^5 < M_\star/\mathrm{M}_\odot < 10^7$. Testing this will require large volume surveys like SDSS to avoid contamination from groups.

(ii) Secondly, below $M_\star \sim 10^5$ $\mathrm{M}_\odot$, we may see the first signs of star formation truncation due to reionization. The smoking gun for this would be an extremely isolated quenched dwarf. However, as discussed in Geha et al. (2012), to be classified as 'extremely isolated' it would need to be found $\gtrsim 4$ virial radii away from any nearby larger galaxy.

(iii) Thirdly, our results imply that there should be many galaxies like Leo T on the outskirts of the Milky Way and Andromeda just waiting to be found. Extrapolating the Bolshoi mass function to low mass, we predict that there should be ∼2000 galaxies like Leo T in a typical 10 $\mathrm{Mpc}^3$ volume, with halo mass $5 \times 10^8 < M_{200}/\mathrm{M}_\odot < 10^9$, stellar mass $\sim 2 \times 10^5 < M_\star/\mathrm{M}_\odot < 6 \times 10^5$, and H I gas mass $\sim 3 \times 10^5 < M_{\mathrm{HI}}/\mathrm{M}_\odot < 3 \times 10^6$. In practice, this will be an upper bound because many of these 'Leo T'-like dIrrs will have been ram pressure stripped by a nearby host galaxy. Nonetheless, it is tantalizing that Leo T lies right on the edge of the SDSS survey footprint (Koposov et al. 2009). Any closer to the Milky Way and Leo T would have been stripped of its gas, similarly to the recently discovered Eridanus II galaxy (Crnojević et al. 2016). Any further away, and it would have been too faint to be seen. Indeed, James et al. (2017) have recently discovered a slew of new star-forming dIrrs in the Local Volume. These may be the tip of the iceberg.

Finally, we note that the comparison between $M_\star$–$M_{200}|_{\mathrm{abund}}$ and $M_\star$–$M_{200}|_{\mathrm{rot}}$ shows great promise for constraining $m_{\mathrm{WDM}}$ if we can reach down to Leo T mass galaxies and below. This suggests that it is worth the effort of attempting to model the Local Group at the fidelity of the simulations presented in R16a, despite the computational challenges that this presents. At least some of the 'ultra-faint' dwarfs that have already been found orbiting the Milky Way and Andromeda are likely even less massive than Leo T (e.g. Kirby et al. 2013a), holding the promise of providing unparalleled constraints on $m_{\mathrm{WDM}}$ and/or other cosmologies that suppress small-scale power.

## 7 CONCLUSIONS

We have presented a clean probe of cosmology on small scales that follows from the comparison of $M_\star$–$M_{200}|_{\mathrm{rot}}$, measured from the rotation curves of isolated dwarf galaxies in the field, and $M_\star$–$M_{200}|_{\mathrm{abund}}$ calculated from abundance matching (see Section 2). These should agree if the cosmological model is correct, but will diverge if the halo mass function is too shallow or steep on small scales. Our probe is comparatively clean since it relies only on the following theory ingredients: (i) a monotonic relation between stellar mass and halo mass, (ii) a predicted dark matter halo mass function and (iii) a robust prediction of the internal dark matter distribution in dIrrs, for a given cosmological model. The first of these can be empirically tested using $M_\star$–$M_{200}|_{\mathrm{rot}}$, while (ii) and (iii) are readily obtained from state-of-the art numerical simulations (see Section 2).

Our key results are as follows.

(i) We fit the rotation curves of a carefully selected sample of 19 isolated dIrr galaxies. Of these, five were found to be of too low inclination to be reliably inclination corrected ('inclination rogues'), another two (DDO 216 and NGC 1569) showed clear signs of disequilibrium ('disequilibrium rogues'), while one (DDO 101) had a very large distance uncertainty ('distance rogues'). For the remaining 11 dIrrs, we found that an NFW dark matter halo profile is ruled out at 99 per cent confidence, reaffirming the well-known 'cusp-core' problem. By contrast, the coreNFW profile from R16a – that accounts for cusp-core transformations due to stellar feedback – gives an excellent fit in all cases, without introducing any more free parameters than the NFW form.

(ii) Although we required the coreNFW profile to obtain a good fit to the rotation curve shape, we showed that the implied dark matter halo mass $M_{200}$ was not sensitive to the form of the dark matter density profile within $r \lesssim R_{1/2}$. For this reason, we were able to robustly measure the stellar mass–halo mass relation $M_\star$–$M_{200}|_{\mathrm{rot}}$ over the mass range $5 \times 10^5 \lesssim M_\star/\mathrm{M}_\odot \lesssim 10^8$, finding a monotonic relation with little scatter.

(iii) Such monotonicity implies that abundance matching should yield a $M_\star$–$M_{200}|_{\mathrm{abund}}$ relation that matches $M_\star$–$M_{200}|_{\mathrm{rot}}$, if the cosmological model is correct. Using the 'field galaxy' stellar mass function from the SDSS and the halo mass function from the ΛCDM Bolshoi simulation, we found remarkable agreement between the two. This held down to $M_{200} \sim 5 \times 10^9$ $\mathrm{M}_\odot$, and to $M_{200} \sim 5 \times 10^8$ $\mathrm{M}_\odot$ if we assumed a power-law extrapolation of the SDSS stellar mass function below $M_\star \sim 10^7$ $\mathrm{M}_\odot$.

(iv) The good agreement between $M_\star$–$M_{200}|_{\mathrm{rot}}$ and $M_\star$–$M_{200}|_{\mathrm{abund}}$ means that there is no 'missing satellites' or TBTF problem for our sample of isolated dIrrs down to at least $M_{200} \sim 5 \times 10^9$ $\mathrm{M}_\odot$. This is lower than the mass scale at which the 'missing satellites' and TBTF problems manifest in the Local Group, $M_{\mathrm{TBTF}} \sim 10^{10}$ $\mathrm{M}_\odot$ (e.g. Read et al. 2006; Boylan-Kolchin et al. 2011; Tollerud et al. 2014). This suggests that both problems depend on *environment* and therefore owe to 'galaxy formation physics' rather than exotic cosmology.

(v) Compiling stellar mass functions from the literature, we showed that the group stellar mass function is substantially shallower than the field below $M_\star \sim 10^9$ $\mathrm{M}_\odot$. We argued that this likely owes to ram-pressure stripping on group infall. This induces a significant scatter in $M_\star$ for a given pre-infall $M_{200}$ causing classical abundance matching to fail.

(vi) We considered how well a ΛWDM cosmology can fit $M_\star$–$M_{200}|_{\mathrm{rot}}$. Repeating our abundance matching using the SDSS field stellar mass function, we showed that ΛWDM fails at 68 per cent confidence for a thermal relic mass of $m_{\mathrm{WDM}} < 1.25$ keV, and $m_{\mathrm{WDM}} < 2$ keV if we used the power-law extrapolation of the SDSS stellar mass function.

(vii) If ΛCDM is correct, we predict that the stellar mass function of galaxies should continue as an unbroken power law with slope $\alpha \sim 1.6$, at least over the mass range $10^5 < M_\star/\mathrm{M}_\odot < 10^7$. There should be ∼2000 galaxies like Leo T in a typical 10 $\mathrm{Mpc}^3$ volume, with halo mass $5 \times 10^8 < M_{200}/\mathrm{M}_\odot < 10^9$, stellar mass $\sim 2 \times 10^5 < M_\star/\mathrm{M}_\odot < 6 \times 10^5$, and H I gas mass $\sim 3 \times 10^5 < M_{\mathrm{HI}}/\mathrm{M}_\odot < 3 \times 10^6$. Below this mass scale, we may see the first signs of star formation suppression due to reionization.

## ACKNOWLEDGEMENTS

JIR and OA would like to acknowledge support from STFC consolidated grant ST/M000990/1. JIR acknowledges support from the MERAC foundation. OA would like to acknowledge support from the Swedish Research Council (grant 2014-5791). This research made use of APLpy, an open-source plotting package for Python hosted at http://aplpy.github.com. This work used PyNbody for the simulation analysis (https://github.com/pynbody/pynbody; Pontzen et al. 2013). All simulations were run on the Surrey Galaxy Factory. We would like to thank Se-Heon Oh and Little THINGS for

kindly making their data public, and Erwin de Blok for providing the data for NGC 6822. We would like to thank Andrew Pontzen, Julio Navarro, Kyle Oman, Peter Behroozi and Annika Peter for useful discussions. We would like to thank the anonymous referee for useful comments that improved the clarity of this work.

## REFERENCES

Agertz O., Kravtsov A. V., 2016, ApJ, 824, 79
Anderhalden D., Schneider A., Macciò A. V., Diemand J., Bertone G., 2013, J. Cosmol. Astropart. Phys., 3, 014
Angulo R. E., Hahn O., Abel T., 2013, MNRAS, 434, 3337
Ashley T., Simpson C. E., Elmegreen B. G., 2013, AJ, 146, 42
Avila-Reese V., Colín P., Valenzuela O., D'Onghia E., Firmani C., 2001, ApJ, 559, 516
Baldry I. K., Glazebrook K., Driver S. P., 2008, MNRAS, 388, 945
Baldry I. K. et al., 2012, MNRAS, 421, 621
Barnard E. E., 1884, Astron. Nachr., 110, 125
Baugh C. M., 2006, Rep. Progress Phys., 69, 3101
Baur J., Palanque-Delabrouille N., Yèche C., Magneville C., Viel M., 2016, JCAP, 08, 012
Behroozi P. S., Conroy C., Wechsler R. H., 2010, ApJ, 717, 379
Behroozi P. S., Wechsler R. H., Conroy C., 2013, ApJ, 770, 57
Bigiel F. et al., 2011, ApJ, 730, L13
Binney J., Tremaine S., 2008, Galactic Dynamics. Princeton University Press, Princeton, NJ
Blake C., Glazebrook K., 2003, ApJ, 594, 665
Bland-Hawthorn J., Sutherland R., Webster D., 2015, ApJ, 807, 154
Blandford R. D., Saust A. B., Brainerd T. G., Villumsen J. V., 1991, MNRAS, 251, 600
Blanton M. R. et al., 2001, AJ, 121, 2358
Blanton M. R. et al., 2003, ApJ, 592, 819
Blanton M. R., Lupton R. H., Schlegel D. J., Strauss M. A., Brinkmann J., Fukugita M., Loveday J., 2005, ApJ, 631, 208
Bode P., Ostriker J. P., Turok N., 2001, ApJ, 556, 93
Bolzonella M. et al., 2010, A&A, 524, A76
Boyarsky A., Lesgourgues J., Ruchayskiy O., Viel M., 2009, J. Cosmol. Astropart. Phys., 5, 12
Boylan-Kolchin M., Bullock J. S., Kaplinghat M., 2011, MNRAS, 415, L40
Brook C. B., Shankar F., 2016, MNRAS, 455, 3841
Brook C. B., Di Cintio A., Knebe A., Gottlöber S., Hoffman Y., Yepes G., Garrison-Kimmel S., 2014, ApJ, 784, L14
Brooks A. M., Kuhlen M., Zolotov A., Hooper D., 2013, ApJ, 765, 22
Cacciato M., van den Bosch F. C., More S., Li R., Mo H. J., Yang X., 2009, MNRAS, 394, 929
Carollo C. M. et al., 2013, ApJ, 776, 71
Chabrier G., 2003, PASP, 115, 763
Chan T. K., Kereš D., Oñorbe J., Hopkins P. F., Muratov A. L., Faucher-Giguère C.-A., Quataert E., 2015, MNRAS, 454, 2981
Crnojević D., Sand D. J., Zaritsky D., Spekkens K., Willman B., Hargis J. R., 2016, ApJ, 824, L14
Crocce M. et al., 2016, MNRAS, 455, 4301
Croft R. A. C., Weinberg D. H., Katz N., Hernquist L., 1998, ApJ, 495, 44
D'Onghia E., Springel V., Hernquist L., Keres D., 2010, ApJ, 709, 1138
Dawson K. S. et al., 2013, AJ, 145, 10
de Blok W. J. G., Bosma A., 2002, A&A, 385, 816
de Blok W. J. G., Walter F., 2000, ApJ, 537, L95
de Boer T. J. L., Tolstoy E., Lemasle B., Saha A., Olszewski E. W., Mateo M., Irwin M. J., Battaglia G., 2014, A&A, 572, A10
Dehnen W., Read J. I., 2011, Eur. Phys. J. Plus, 126, 55
del Pino A., Hidalgo S. L., Aparicio A., Gallart C., Carrera R., Monelli M., Buonanno R., Marconi G., 2013, MNRAS, 433, 1505
Di Cintio A., Brook C. B., Dutton A. A., Macciò A. V., Stinson G. S., Knebe A., 2014, MNRAS, 441, 2986
Di Teodoro E. M., Fraternali F., 2015, MNRAS, 451, 3021
Diemand J., Kuhlen M., Madau P., 2007, ApJ, 667, 859
Driver S. P. et al., 2011, MNRAS, 413, 971
Eckert K. D., Kannappan S. J., Stark D. V., Moffett A. J., Berlind A. A., Norris M. A., 2016, ApJ, 824, 124
Eisenstein D. J. et al., 2005, ApJ, 633, 560
El-Badry K., Wetzel A. R., Geha M., Quataert E., Hopkins P. F., Kereš D., Chan T. K., Faucher-Giguère C.-A., 2017, ApJ, 835, 193
Elbert O. D., Bullock J. S., Garrison-Kimmel S., Rocha M., Oñorbe J., Peter A. H. G., 2015, MNRAS, 453, 29
Ferrero I., Abadi M. G., Navarro J. F., Sales L. V., Gurovich S., 2012, MNRAS, 425, 2817
Finoguenov A. et al., 2007, ApJS, 172, 182
Fitts A. et al., 2016, MNRAS, preprint (arXiv:1611.02281)
Flores R. A., Primack J. R., 1994, ApJ, 427, L1
Foreman-Mackey D., Hogg D. W., Lang D., Goodman J., 2013, PASP, 125, 306
Fu L. et al., 2014, MNRAS, 441, 2725
Garrison-Kimmel S., Rocha M., Boylan-Kolchin M., Bullock J. S., Lally J., 2013, MNRAS, 433, 3539
Garrison-Kimmel S., Boylan-Kolchin M., Bullock J. S., Kirby E. N., 2014, MNRAS, 444, 222 (G-K14)
Garrison-Kimmel S., Bullock J. S., Boylan-Kolchin M., Bardwell E., 2017, MNRAS, 464, 3108
Gatto A., Fraternali F., Read J. I., Marinacci F., Lux H., Walch S., 2013, MNRAS, 433, 2749
Geha M., Blanton M. R., Yan R., Tinker J. L., 2012, ApJ, 757, 85
Giodini S. et al., 2012, A&A, 538, A104
Gnedin N. Y., 2016, ApJ, 821, 50
Gnedin N. Y., Kaurov A. A., 2014, ApJ, 793, 30
Gnedin O. Y., Zhao H., 2002, MNRAS, 333, 299
Górski M., Pietrzyński G., Gieren W., 2011, AJ, 141, 194
Grebel E. K., Gallagher J. S., Harbeck D., 2003, AJ, 125, 1926
Haardt F., Madau P., 2012, ApJ, 746, 125
Hague P. R., Wilkinson M. I., 2013, MNRAS, 433, 2314
Hahn O., Abel T., Kaehler R., 2013, MNRAS, 434, 1171
Haynes M. P., Giovanelli R., Chincarini G. L., 1984, ARA&A, 22, 445
Hobbs A., Read J., Agertz O., Iannuzzi F., Power C., 2016, MNRAS, 458, 468
Iorio G., Fraternali F., Nipoti C., Di Teodoro E., Read J. I., Battaglia G., 2016, MNRAS, preprint (arXiv:1611.03865)
Irwin M., Hatzidimitriou D., 1995, MNRAS, 277, 1354
James B. L., Koposov S. E., Stark D. P., Belokurov V., Pettini M., Olszewski E. W., McQuinn K. B. W., 2017, MNRAS, 465, 3977
Jethwa P., Belokurov V., Erkal D., 2016, MNRAS, preprint (arXiv:1612.07834)
Johnson M., Hunter D. A., Oh S.-H., Zhang H.-X., Elmegreen B., Brinks E., Tollerud E., Herrmann K., 2012, AJ, 144, 152
Katz H., Lelli F., McGaugh S. S., Di Cintio A., Brook C. B., Schombert J. M., 2017, MNRAS, 466, 1648
Kauffmann G., 2014, MNRAS, 441, 2717
Kazantzidis S., Łokas E. L., Mayer L., 2013, ApJ, 764, L29
Kepley A. A., Wilcots E. M., Hunter D. A., Nordgren T., 2007, AJ, 133, 2242
Kimm T., Cen R., 2014, ApJ, 788, 121
Kirby E. N., Boylan-Kolchin M., Cohen J. G., Geha M., Bullock J. S., Kaplinghat M., 2013a, ApJ, 770, 16
Kirby E. N., Cohen J. G., Guhathakurta P., Cheng L., Bullock J. S., Gallazzi A., 2013b, ApJ, 779, 102
Klypin A., Kravtsov A. V., Valenzuela O., Prada F., 1999, ApJ, 522, 82
Klypin A. A., Trujillo-Gomez S., Primack J., 2011, ApJ, 740, 102
Klypin A., Karachentsev I., Makarov D., Nasonova O., 2015, MNRAS, 454, 1798
Koposov S. E., Yoo J., Rix H.-W., Weinberg D. H., Macciò A. V., Escudé J. M., 2009, ApJ, 696, 2179
Kravtsov A. V., 2013, ApJ, 764, L31
Kuzio de Naray R., Kaufmann T., 2011, MNRAS, 414, 3617
Leaman R. et al., 2012, ApJ, 750, 33
Lelli F., Verheijen M., Fraternali F., 2014, A&A, 566, A71
Lilly S. J. et al., 2007, ApJS, 172, 70
Łokas E. L., Kazantzidis S., Mayer L., 2012, ApJ, 751, L15

Lovell M. R., Frenk C. S., Eke V. R., Jenkins A., Gao L., Theuns T., 2014, MNRAS, 439, 300
Lux H., Read J. I., Lake G., 2010, MNRAS, 406, 2312
Macciò A. V., Dutton A. A., van den Bosch F. C., Moore B., Potter D., Stadel J., 2007, MNRAS, 378, 55
Macciò A. V., Kang X., Fontanot F., Somerville R. S., Koposov S., Monaco P., 2010, MNRAS, 402, 1995
McConnachie A. W., 2012, AJ, 144, 4
McQuinn K. B. W. et al., 2010, ApJ, 721, 297
McQuinn K. B. W., Lelli F., Skillman E. D., Dolphin A. E., McGaugh S. S., Williams B. F., 2015, MNRAS, 450, 3886
Madau P., Shen S., Governato F., 2014, ApJ, 789, L17
Makarov D., Karachentsev I., 2011, MNRAS, 412, 2498
Makarova L., 1999, A&AS, 139, 491
Martin N. F., de Jong J. T. A., Rix H.-W., 2008, ApJ, 684, 1075
Mateo M. L., 1998, ARA&A, 36, 435
Mayer L., Governato F., Colpi M., Moore B., Quinn T., Wadsley J., Stadel J., Lake G., 2001a, ApJ, 547, L123
Mayer L., Governato F., Colpi M., Moore B., Quinn T., Wadsley J., Stadel J., Lake G., 2001b, ApJ, 559, 754
Menci N., Grazian A., Castellano M., Sanchez N. G., 2016, ApJ, 825, L1
Miller S. H., Ellis R. S., Newman A. B., Benson A., 2014, ApJ, 782, 115
Moore B., 1994, Nature, 370, 629
Moore B., Ghigna S., Governato F., Lake G., Quinn T., Stadel J., Tozzi P., 1999, ApJ, 524, L19
Moster B. P., Somerville R. S., Maulbetsch C., van den Bosch F. C., Macciò A. V., Naab T., Oser L., 2010, ApJ, 710, 903
Muñoz R. R. et al., 2006, ApJ, 649, 201
Navarro J. F., Eke V. R., Frenk C. S., 1996a, MNRAS, 283, L72
Navarro J. F., Frenk C. S., White S. D. M., 1996b, ApJ, 462, 563
Ocvirk P. et al., 2016, MNRAS, 463, 1462
Oh S.-H., Brook C., Governato F., Brinks E., Mayer L., de Blok W. J. G., Brooks A., Walter F., 2011, AJ, 142, 24
Oh S.-H. et al., 2015, AJ, 149, 180
Oñorbe J., Boylan-Kolchin M., Bullock J. S., Hopkins P. F., Kerěs D., Faucher-Giguère C.-A., Quataert E., Murray N., 2015, MNRAS, 454, 2092
Pace A. B., 2016, MNRAS, preprint (arXiv:1605.05326) (P16)
Papastergis E., Shankar F., 2016, A&A, 591, A58
Papastergis E., Giovanelli R., Haynes M. P., Shankar F., 2015, A&A, 574, A113
Peacock J. A., 1999, Cosmological Physics. Cambridge University Press, Cambridge, UK
Peñarrubia J., Benson A. J., Walker M. G., Gilmore G., McConnachie A. W., Mayer L., 2010, MNRAS, 406, 1290
Peñarrubia J., Pontzen A., Walker M. G., Koposov S. E., 2012, ApJ, 759, L42
Peñarrubia J., Gómez F. A., Besla G., Erkal D., Ma Y.-Z., 2016, MNRAS, 456, L54
Peng Y.-j. et al., 2010, ApJ, 721, 193
Peng Y.-j., Lilly S. J., Renzini A., Carollo M., 2012, ApJ, 757, 4
Planck Collaboration XVI, 2014, A&A, 571, A16
Pontzen A., Governato F., 2012, MNRAS, 421, 3464
Pontzen A., Governato F., 2014, Nature, 506, 171
Pontzen A., Roškar R., Stinson G., Woods R., 2013, pynbody: *N*-body/SPH Analysis for python, Astrophysics Source Code Library, record ascl:1305.002
Pontzen A., Read J., Teyssier R., Governato F., Gualandris A., Roth N., Devriendt J., 2015, MNRAS, 451, 1366
Puche D., Westpfahl D., Brinks E., Roy J.-R., 1992, AJ, 103, 1841
Read J. I., 2014, J. Phys. G Nuclear Phys., 41, 063101
Read J. I., Gilmore G., 2005, MNRAS, 356, 107
Read J. I., Trentham N., 2005, R. Soc. Lond. Phil. Trans. Ser. A, 363, 2693 (RT05)
Read J. I., Wilkinson M. I., Evans N. W., Gilmore G., Kleyna J. T., 2006, MNRAS, 367, 387
Read J. I., Agertz O., Collins M. L. M., 2016a, MNRAS, 459, 2573 (R16a)
Read J. I., Iorio G., Agertz O., Fraternali F., 2016b, MNRAS, 462, 3628 (R16b)
Ricotti M., 2009, MNRAS, 392, L45
Rocha M., Peter A. H. G., Bullock J. S., Kaplinghat M., Garrison-Kimmel S., Oñorbe J., Moustakas L. A., 2013, MNRAS, 430, 81
Romanowsky A. J., Strader J., Spitler L. R., Johnson R., Brodie J. P., Forbes D. A., Ponman T., 2009, AJ, 137, 4956
Ryan-Weber E. V., Begum A., Oosterloo T., Pal S., Irwin M. J., Belokurov V., Evans N. W., Zucker D. B., 2008, MNRAS, 384, 535
Sánchez-Salcedo F. J., Hidalgo-Gámez A. M., Martínez-García E. E., 2014, Rev. Mex. Astron. Astrofis., 50, 225
Sawala T. et al., 2016a, MNRAS, 456, 85
Sawala T. et al., 2016b, MNRAS, 457, 1931
Schneider A., Smith R. E., Macciò A. V., Moore B., 2012, MNRAS, 424, 684
Shan H. et al., 2015, MNRAS, preprint (arXiv:1502.00313)
Shibuya T., Ouchi M., Harikane Y., 2015, ApJS, 219, 15
Silich S., Lozinskaya T., Moiseev A., Podorvanuk N., Rosado M., Borissova J., Valdez-Gutierrez M., 2006, A&A, 448, 123
Simpson C. M., Bryan G. L., Johnston K. V., Smith B. D., Mac Low M.-M., Sharma S., Tumlinson J., 2013, MNRAS, 432, 1989
Smoot G. F. et al., 1992, ApJ, 396, L1
Springel V., Frenk C. S., White S. D. M., 2006, Nature, 440, 1137
Stewart K. R., Bullock J. S., Barton E. J., Wechsler R. H., 2009, ApJ, 702, 1005
Swaters R. A., 1999, PhD thesis, Rijksuniversiteit Groningen
Teyssier R., Pontzen A., Dubois Y., Read J. I., 2013, MNRAS, 429, 3068
Tollerud E. J., Boylan-Kolchin M., Bullock J. S., 2014, MNRAS, 440, 3511
Tollet E. et al., 2016, MNRAS, 456, 3542
Tolstoy E., Hill V., Tosi M., 2009, ARA&A, 47, 371
Tomozeiu M., Mayer L., Quinn T., 2016, ApJ, 827, L15
Trebitsch M., Blaizot J., Rosdahl J., 2015, in Martins F., Boissier S., Buat V., Cambrésy L., Petit P., eds, SF2A-2015: Modeling Small Galaxies During the Epoch of Reionisation. Astronomy and Astrophysics Library. Springer, New York, p. 105
Trentham N., 1998, MNRAS, 294, 193
Trentham N., Tully R. B., 2002, MNRAS, 335, 712
Trentham N., Sampson L., Banerji M., 2005, MNRAS, 357, 783
Trujillo-Gomez S., Schneider A., Papastergis E., Reed D. S., Lake G., 2016, preprint, (arXiv:1610.09335)
Ural U., Wilkinson M. I., Read J. I., Walker M. G., 2015, Nature Commun., 6, 7599
Vale A., Ostriker J. P., 2004, MNRAS, 353, 189
van der Marel R. P., Alves D. R., Hardy E., Suntzeff N. B., 2002, AJ, 124, 2639
van Eymeren J., Marcelin M., Koribalski B., Dettmar R.-J., Bomans D. J., Gach J.-L., Balard P., 2009, A&A, 493, 511
Vandenbroucke B., Verbeke R., De Rijcke S., 2016, MNRAS, 458, 912
Wang J., White S. D. M., 2007, MNRAS, 380, 93
Warren S. R. et al., 2011, ApJ, 738, 10
Weisz D. R. et al., 2012a, ApJ, 744, 44
Weisz D. R. et al., 2012b, ApJ, 748, 88
Weldrake D. T. F., de Blok W. J. G., Walter F., 2003, MNRAS, 340, 12
Wetzel A. R., Hopkins P. F., Kim J.-h., Faucher-Giguere C.-A., Keres D., Quataert E., 2016, ApJ, 827, L23
Wheeler C., Onorbe J., Bullock J. S., Boylan-Kolchin M., Elbert O., Garrison-Kimmel S., Hopkins P. F., Keres D., 2015, MNRAS, 453, 1305
Xia L., Zhou X., Yang Y., Ma J., Jiang Z., 2006, ApJ, 652, 249
Yang X., Mo H. J., van den Bosch F. C., 2009, ApJ, 695, 900
Zentner A. R., Bullock J. S., 2002, Phys. Rev. D, 66, 43003
Zhang Z., Xu H., Wang Y., An T., Xu Y., Wu X.-P., 2007, ApJ, 656, 805
Zhang H.-X., Hunter D. A., Elmegreen B. G., Gao Y., Schruba A., 2012, AJ, 143, 47
Zhu Q., Marinacci F., Maji M., Li Y., Springel V., Hernquist L., 2016, MNRAS, 458, 1559
Zolotov A. et al., 2012, ApJ, 761, 71

## APPENDIX A: THE ROTATION CURVE FITS

In this Appendix, we show the rotation curves and model fits for all of the galaxies listed in Table 2. In Figs A1 and A2, we show all of the galaxies that we include in Fig. 3; in Fig. A3, we show all of the 'rogues' that we exclude from further analysis. The rogues fall into three categories: 'inclination' $i$-Rogues (top row); 'disequilibrium' Diseq. Rogues (middle row) and 'distance' $D$-Rogues (bottom row), as marked (see Section 4.4). The first class of these three have uncertain inclination, with $i_{\rm fit} < 40^{\circ}$. The second class show signs of disequilibrium, either in the form of significant fast-expanding H I bubbles (see Table 2), or – as is the case for Pegasus – because we only have data for the inner rotation curve inside $R_{1/2}$. This inner region is particularly susceptible to disequilibrium effects from both supernova-driven H I holes and non-circular motions. (This can be seen, for example, in the inner rotation curves of NGC 6822 and DDO 126 that are otherwise both in our 'good' sample.) The third class (which contains only DDO 101) have very uncertain distance $D$ (see R16b for a detailed discussion of this galaxy.). The individual galaxies are discussed in more detail in Iorio et al. (2016) where we present the full details of our rotation curve derivation, including a comparison with the rotation curves from Little THINGS.

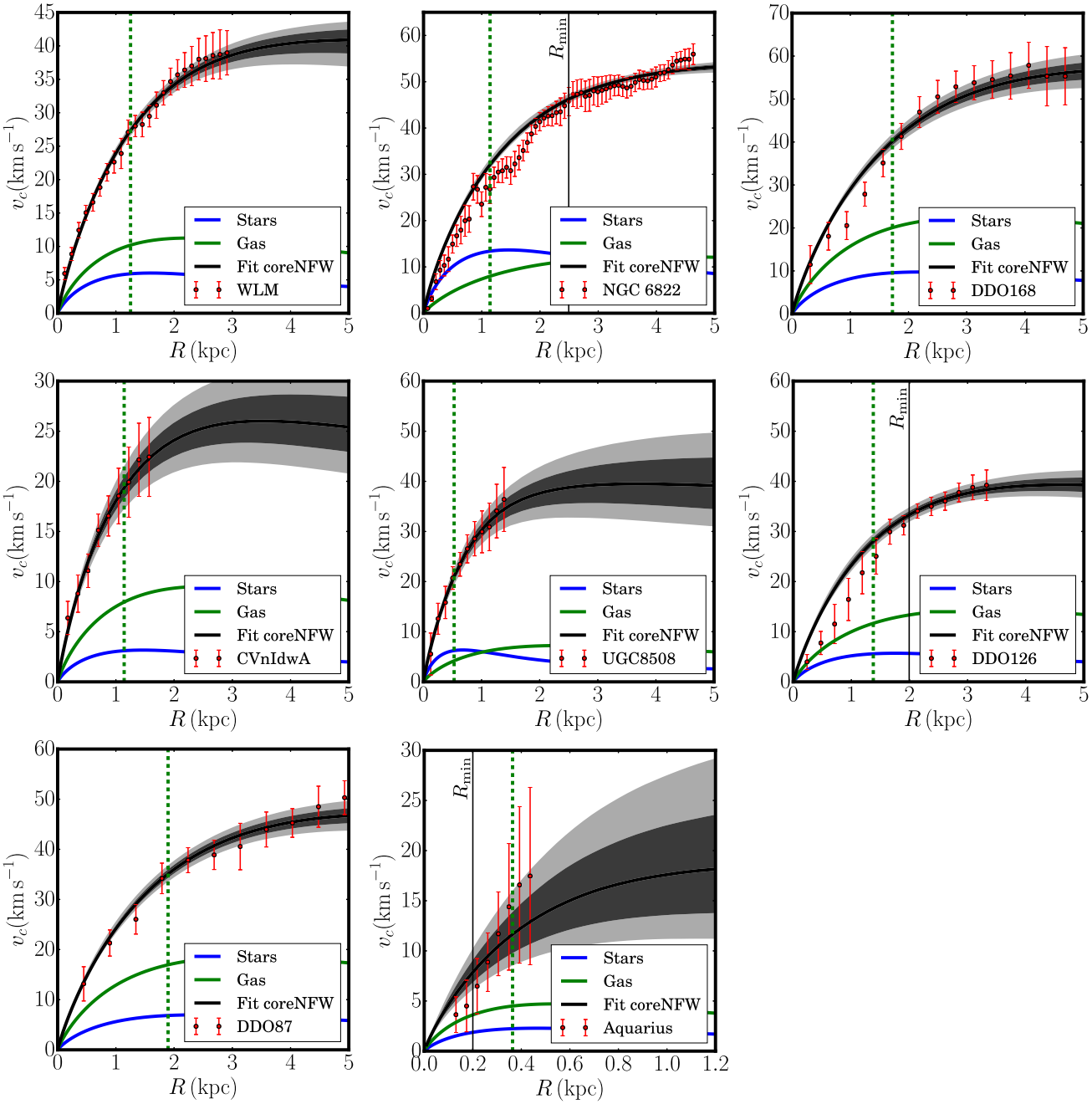


**Figure A1.** Rotation curve data (red data points) and models for our sample of 'good' dIrr galaxies (see Table 2). The black contours show the median (black), 68 per cent (dark grey) and 95 per cent (light grey) confidence intervals of our fitted coreNFW rotation curve models (see Section 4.2). The vertical green dashed line shows the projected stellar half light radius $R_{1/2}$. The thin vertical black line marks the inner data point used for the fit, $R_{\rm min}$ (where this is not marked $R_{\rm min} = 0$). The blue and green lines show the rotation curve contribution from stars and gas, respectively.

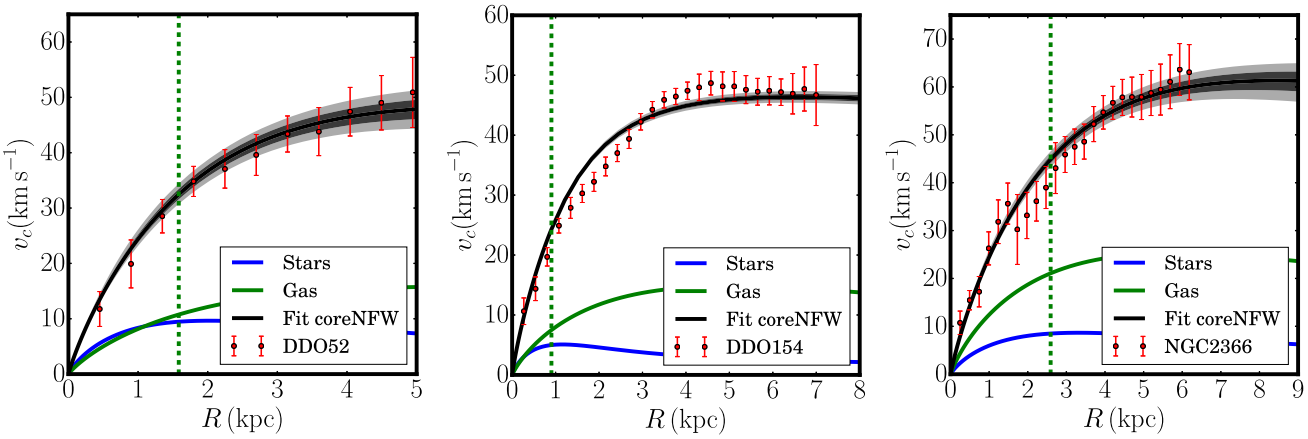


**Figure A2.** Continuation of Fig. A1.

## APPENDIX B: TESTING THE ROBUSTNESS OF OUR $M_\star$–$M_{200}|_{\rm rot}$ RELATION

In this Appendix, we explore how robust our $M_\star$–$M_{200}|_{\rm rot}$ relation is to key assumptions in our methodology. In Fig. B1, left panel, we show our $M_\star$–$M_{200}|_{\rm rot}$ relation including the *i*-Rogues (blue data points) and *D*-Rogues (magenta data points). Recall that for the *i*-Rogues, we marginalize over the inclination angle with a flat prior over the range $0^\circ < i < 40^\circ$ (see Section 4). In most cases, this significantly inflates the uncertainties. However, DDO 133 has sufficiently good data that – under the assumption of a coreNFW dark matter profile – its rotation curve shape is sufficient to provide a measurement of *i* (see Fig. A3).

As can be seen in Fig. B1, left panel, including the *i*-Rogues introduces substantially more scatter about the $M_\star$–$M_{200}|_{\rm rot}$ relation, but no more than is expected given their larger uncertainties on $M_{200}$. Thus, the *i*-Rogues do not substantially alter our key results and conclusions. We do, however, find an additional outlier, DDO 50, that appears to have a very high $M_\star$ for its $M_{200}$, even when marginalizing over *i*. As can be seen in Fig. A3, however, DDO 50 has an unusual rotation curve with prominent wiggles out to large radii. This makes it challenging to inclination correct. Indeed, from a stability analysis, Sánchez-Salcedo, Hidalgo-Gámez & Martínez-García (2014) argue for an inclination for DDO 50 of $i = 27^\circ$ that is substantially smaller than the $\sim 37^\circ$ that we find here (see Table 2). This lower inclination would be sufficient to push DDO 50 on to the $M_\star$–$M_{200}|_{\rm rot}$ relation.

Our one *D*-Rogue – DDO 101 – is marked in Fig. B1, left panel, by the magenta data points. Since the distance for this galaxy is highly uncertain (see the discussion in R16b), we plot two points for $D_{\rm DDO101} = 6.4$ Mpc and $D_{\rm DDO101} = 12.9$ Mpc. As can be seen, these straddle the $M_\star$–$M_{200}|_{\rm rot}$ relation. Thus, our *D*-Rogue does not affect our key results and conclusions either.

Finally, we consider the effect of allowing the dark matter core size to freely vary by performing our rotation curve fits assuming a flat prior on $\eta$ (equation 11) over the range $0 < \eta < 2.75$. (The upper bound on $\eta$ is set by the energetic arguments in Section 6.6. There, we showed that the integrated supernova energy is not sufficient to build cores larger than $\sim 2.75 R_{1/2}$; see Fig. 5.) The results for $M_\star$–$M_{200}|_{\rm rot}$ are shown in Fig. B1 (middle panel), while Fig. B1, right panel, shows the marginalized $\eta$ parameters for each galaxy that result from this fit, including the *i*-Rogues (blue data points) and *D*-Rogues (magenta data points). The horizontal black line marks our default $\eta = 1.75$.

From Fig. B1, middle panel, we see that allowing $\eta$ to vary increases our errors on $M_{200}$ but does not otherwise affect our key results or conclusions. This is consistent with our findings in Section 5.1, where we showed that fitting an NFW profile to the rotation curves gives a poorer fit, but does not significantly alter the derived $M_{200}$ within our quoted uncertainties. Finally, from the rightmost panel of Fig. B1, we can see that we do not obtain very strong constraints on $\eta$, similarly to our findings for WLM in R16b. The data are consistent with our default $\eta = 1.75$, with perhaps a hint that the more massive galaxies (with $M_{200} \gtrsim 10^{10}\,\mathrm{M}_\odot$) favour a slightly larger core. For our sample of 'good' dIrrs (purple data points), we can definitively rule out a cusp ($\eta = 0$) at greater than 99 per cent confidence.

## APPENDIX C: COMPARISON WITH OTHER ABUNDANCE MATCHING WORK IN THE LITERATURE

In this Appendix, we compare our abundance matching curves in Fig. 3 with other determinations in the literature from Moster et al. (2010), Brook et al. (2014), G-K14 and Garrison-Kimmel et al. (2017). Moster et al. (2010) perform a parametric 'classical' abundance matching of SDSS galaxies in ΛCDM down to $M_{200} \sim 3 \times 10^{10}\,\mathrm{M}_\odot$. Below this mass scale, the extrapolation of the Moster et al. (2010) relation diverges from our abundance matching curve shown in blue. However, this extrapolation is not supported by the latest data from SDSS. Over the mass range $7 \times 10^9 < M_{200}/\mathrm{M}_\odot < 3 \times 10^{10}$, our relation (that is based on deeper SDSS data than Moster et al. 2010; see Behroozi et al. 2010, 2013) diverges significantly from the Moster et al. (2010) extrapolation, suggesting that the Moster et al. (2010) relation should not be used below $M_{200} \sim 3 \times 10^{10}\,\mathrm{M}_\odot$.

Brook et al. (2014) (black data points) and G-K14 (solid black line) reach to much lower stellar mass than SDSS by using constrained simulations of the Local Volume in ΛCDM abundance-matched to Local Group galaxies. In this sense, they are both similar to abundance matching with the group stellar mass function of RT05. In particular, both studies – like our RT05 analysis – rely on the assumption that the Local Group satellites have a monotonic relation between stellar mass and halo mass. Thus, it is perhaps not surprising that Brook et al. (2014), G-K14 and RT05 all agree within their 95 per cent confidence intervals. All

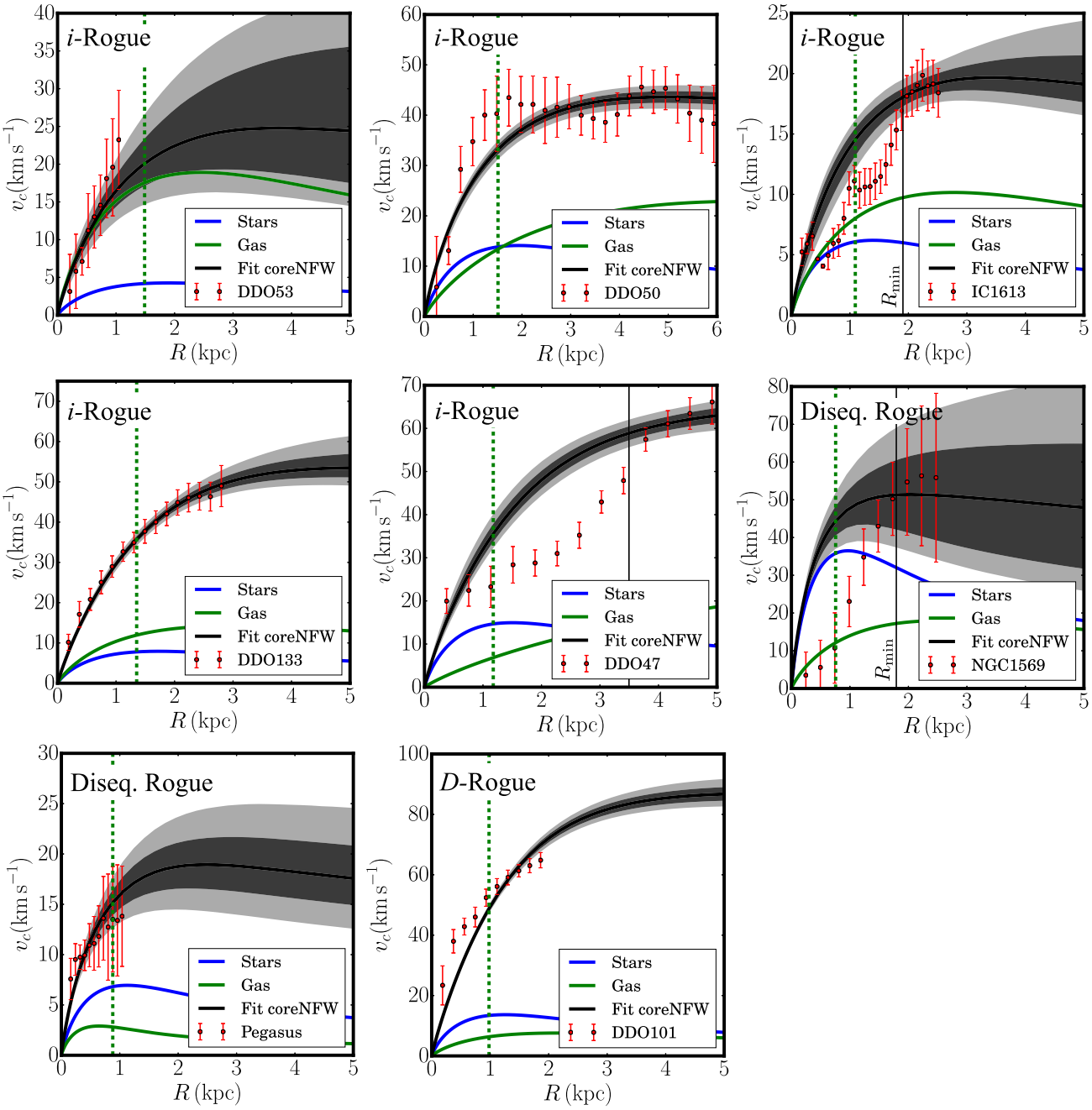


**Figure A3.** Rotation curve data and models for our 'rogue' dIrr galaxies (see Table 2). The lines and symbols are as in Fig. A1. The rogue galaxies fall into three categories: 'inclination' *i*-Rogues, 'disequilibrium' Diseq. Rogues and 'distance' *D*-Rogues, as marked.

three are substantially steeper than the SDSS abundance matching curve (blue). We argued in Sections 5.4 and 6.2 that the assumption of monotonicity is expected to break down inside groups (see also Ural et al. 2015). Indeed, the poor correspondence between the group abundance matching $M_\star$–$M_{200}|_{\rm abund}$ and $M_\star$–$M_{200}|_{\rm rot}$ is evidence for this. Thus, we conclude that, similarly to our RT05 abundance matching relation, the G-K14 and Brook et al. (2014) relations are likely flawed due to the erroneous assumption of monotonicity.

Finally, Garrison-Kimmel et al. (2017) explore relaxing the monotonicity assumption for Local Group galaxies by adding significant scatter to the stellar mass–halo mass relation below some stellar mass scale. This results in the much shallower relation shown by the black dashed line in Fig. C1. This gives a good agreement with our SDSS abundance matching relation (blue lines) and $M_\star$–$M_{200}|_{\rm rot}$ (purple data points), suggesting that such more advanced abundance matching is a promising avenue for probing ΛCDM in group environments.

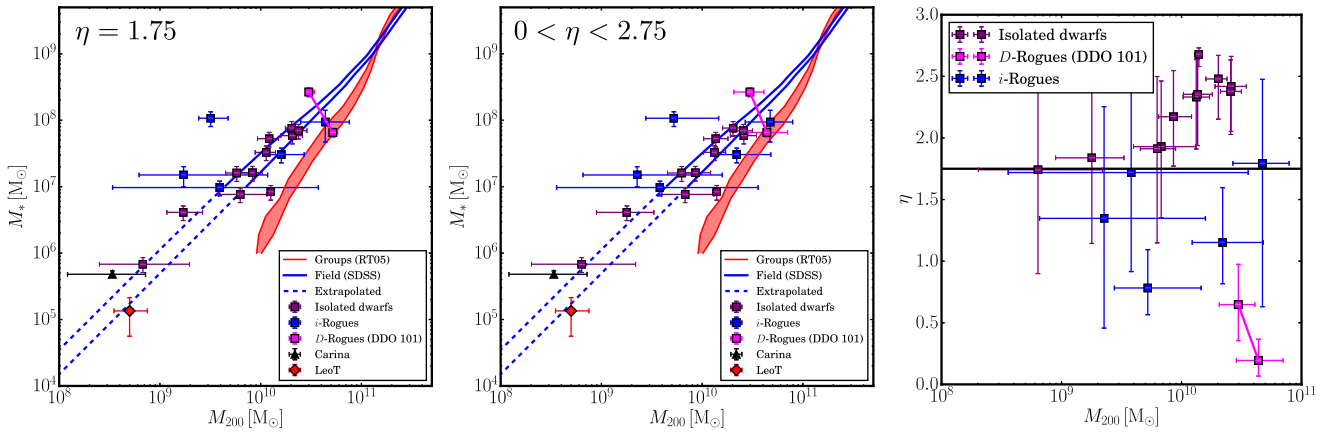


**Figure B1.** Testing the robustness of our $M_\star$–$M_{200}|_{\rm rot}$ relation. In the left panel, we show $M_\star$–$M_{200}|_{\rm rot}$ including the *i*-Rogues (blue data points) and *D*-Rogues (magenta data points); the lines and symbols are as in Fig. 3. In the middle panel, we show the same but now marginalizing over the dark matter core size, using a flat prior on $0 < \eta < 2.75$ (see equation 11). In the right panel, we show the marginalized $\eta$ parameters for each galaxy that result from this fit, including the *i*-Rogues (blue data points) and *D*-Rogues (magenta data points). The horizontal black line marks our default $\eta = 1.75$.

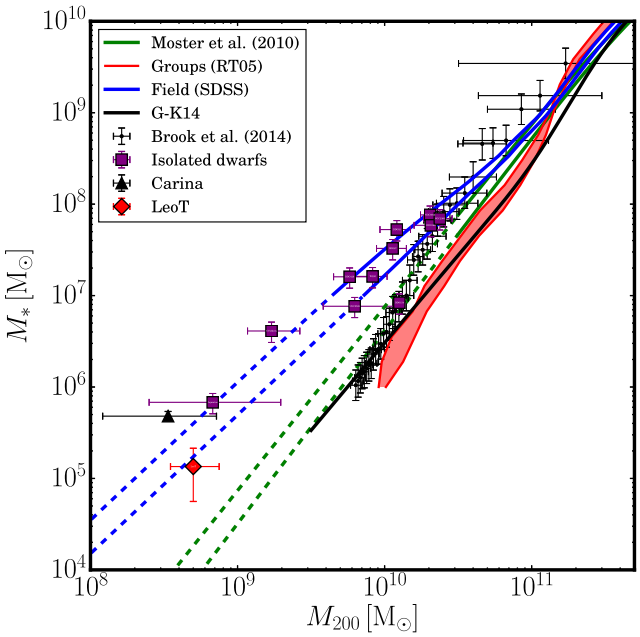


**Figure C1.** A comparison of different abundance matching curves from the literature. The lines and symbols are as in Fig. 3, but we include abundance matching curves from Moster et al. (2010) (green), Brook et al. (2014) (black data points), G-K14 (black solid line).

This paper has been typeset from a TEX/LATEX file prepared by the author.